

1 Effects of super-powerful tropospheric Western Pacific phenomenon 2 of September–October 2018 on ionosphere over China: Results from 3 oblique sounding

4 Leonid F. Chernogor^{1,2,3}, Kostiantyn P. Garmash¹, Qiang Guo², Victor T. Rozumenko¹, Yu Zheng³

5 ¹V. N. Karazin Kharkiv National University, Kharkiv, 61022, Ukraine

6 e-mail: Leonid.F.Chernogor@gmail.com

7 e-mail: Garmash@karazin.ua

8 e-mail: vtrozumenko@gmail.com

9 ²Harbin Engineering University, Harbin, 150001, China

10 e-mail: guoqiang@hrbeu.edu.cn

11 ³Qingdao University, Qingdao, 266071, China

12 e-mail: zhengyu@qdu.edu.cn

13 Correspondence to: Yu Zheng (zhengyu@qdu.edu.cn)

14 **Abstract.** Doppler measurements at oblique propagation paths from the City of Harbin, People's Republic of China
15 (PRC), to ten HF radio broadcast stations in the PRC, Japan, Mongolia, and the Republic of Korea captured the response in
16 the ionosphere to the super typhoon Kong-Rey action from 30 September 2018 to 6 October 2018. The Harbin Engineering
17 University coherent software defined radio system accumulates the database containing the complex amplitudes of the radio
18 signals acquired along 14 propagation paths since 2018. The complex amplitudes are used for calculating the temporal
19 dependences of the Doppler spectra and signal amplitudes, and the Doppler spectra are used to plot the Doppler shift as a
20 function of time, $f_D(t)$, for all rays. The scientific objectives of this study are to reveal the possible perturbations caused by
21 the action of typhoon Kong-Rey, and to estimate the magnitudes of wave parameters of the ionospheric plasma and radio
22 signals. The amplitudes, f_{Da} , of the Doppler shift variations were observed to noticeably increase (factor of ~ 2 – 3) on 1–2 and
23 5–6 October 2018, while the 20–120 min periods, T , of the Doppler shift variations suggest that the wavelike disturbances in
24 the ionosphere are caused by atmospheric gravity waves. The periods and amplitudes of quasi-sinusoidal variations in the
25 Doppler shift, which have been determined for all propagation paths, may be used to estimate the amplitudes, δ_{Na} , of quasi-
26 sinusoidal variations in the electron density. Thus, $T \approx 20$ min and $f_{Da} \approx 0.1$ Hz yield $\delta_{Na} \approx 0.4\%$, whereas $T \approx 30$ min and
27 $f_{Da} \approx 0.2$ Hz give $\delta_{Na} \approx 1.2\%$. If $T \approx 60$ min and $f_{Da} \approx 0.5$ Hz, then $\delta_{Na} \approx 6\%$. The periods T are found to change within the
28 15–120 min limits, and the Doppler shift amplitudes, f_{Da} , show variability within the 0.05–0.4 Hz limits.

29 **1 Introduction**

30 A violent tropical cyclone arising in the northwestern Pacific Ocean is termed the typhoon. In record-breaking typhoons, the
31 atmospheric pressure drops down to 870 hPa, while the pressure deficit reaches 140 hPa, and the wind speed attains a
32 maximum of 85 m s^{-1} , with 94 m s^{-1} maximum gusts.

33 Prasad et al. (1975) were the first to ascertain the influence of meteorological processes, namely, tropical cyclones on
34 the ionosphere. Hung and Kuo (1978, 1985) described observations of traveling ionospheric disturbances (TIDs) as the
35 manifestations of the atmospheric gravity waves (AGWs) generated by hurricanes. Krishnam Raju et al. (1981) have studied
36 the influence of infrasound generated by thunderstorms. Observations of AGWs from meteorological origin have been reported
37 elsewhere (Boška and Šauli, 2001; Šindelarova et al., 2009; Chernigovskaya et al., 2015).

38 The coupling between typhoons and the ionosphere and overlying magnetosphere occurs via a range of
39 mechanisms. Observational studies conducted in recent years have shown that typhoons significantly influence the upper
40 atmosphere, including the ionosphere. Recently, theoretical studies on the coupling between the lower and upper
41 atmosphere, which occur through AGWs, have been published as well (Hickey et al., 2001, 2011; Kuester et al., 2008,
42 Gavrilov and Kshevetskii, 2015, Karpov and Kshevetskii, 2017). Such a mechanism for coupling is naturally called the
43 acoustic–gravity mechanism (Chernogor, 2006, 2012).

44 Typhoons are accompanied by water vapor condensation, the development of powerful convective lift, and the
45 appearance of severe thunderstorms (Mikhailova et al., 2000, 2002). Lightning discharges act to generate electromagnetic
46 emissions that may be capable of heating electrons and perturbing the electron density in the ionospheric *D* region
47 (Nickolaenko and Hayakawa, 1995; Chernogor, 2006, 2012). The large enough fluxes of electromagnetic emissions lead to
48 pitch angle scattering of energetic electrons in the radiation belts via wave-particle interaction, and consequently, part of the
49 electrons precipitates into the lower ionosphere (Inan et al., 2007; Voss et al., 1984, 1998; Bortnik et al., 2006). As a result,
50 secondary perturbations in the plasma conductivity ($\sim 100\text{--}150 \text{ km}$ altitude) and in the geomagnetic and electric fields
51 capable of affecting processes in the magnetosphere can arise. Such a mechanism should be considered as an
52 electromagnetic mechanism (Chernogor, 2006, 2012).

53 An increase in the quasi-stationary electric field may be of different origin (Mikhailova et al., 2000; Isaev et al., 2002,
54 2010; Sorokin et al., 2005; Pulinets et al., 2014). Localized $\sim 10^{-9}\text{--}10^{-8} \text{ A m}^{-2}$ electric currents arise within thunderstorm clouds
55 at $10\text{--}15 \text{ km}$ altitude, which disturb the global electric circuit and increase by 1–2 orders of magnitude quasi-sinusoidal electric
56 fields that are mapped to the ionosphere and magnetosphere and affect the motion of high-energy electrons trapped in the
57 radiation belts. Under certain conditions, the precipitation of these electrons may occur into the ionosphere, and a repeated
58 coupling between the subsystems in the ocean–atmosphere–ionosphere–magnetosphere (OAIM) system happen (Chernogor,
59 2006, 2012). This mechanism for coupling may be termed the electric mechanism (Chernogor, 2006, 2012). Thus, powerful
60 typhoons are capable of governing the coupling between the subsystems in the OAIM system.

61 A lot of studies deal with the acoustic–gravity mechanism, and therefore this mechanism has been studied better
62 than the others. The major role AGWs play in coupling different atmospheric regions under the influence of typhoons and
63 hurricanes on the upper atmosphere is discussed by Okuzawa et al. (1986), Xiao et al. (2007), Vanina–Dart et al. (2007),
64 Afraimovich et al. (2008), Polyakova and Perevalova (2011, 2013), Zakharov and Kunitsyn (2012), Suzuki et al. (2013), Chou
65 et al. (2017), Li et al. (2017, 2018), Chum et al. (2018), Zakharov et al. (2019, 2022). These researchers invoked various
66 measurement techniques for probing the ionosphere: GPS technology, ionosondes, rocket techniques, and HF Doppler
67 technique.

68 The manifestations of the ionospheric response to the super typhoons Hagibis, Ling-Ling, Faxai, and Lekima in
69 radio wave characteristics in the 5–10 MHz band have been studied by Chernogor et al. (2021, 2022) and Zheng et al.,
70 (2022). The variations in the main features of radio waves have been determined, and aperiodic and quasi-sinusoidal
71 perturbations in the electron density have been ascertained.

72 The effect of sudden stratospheric warming events, variations in space weather, solar activity, and of AGWs on the
73 coupling between the subsystems in the atmosphere–ionosphere system has been analyzed in the review by Yiğit et al. (2016),
74 whereas twenty years earlier, the review by Hocke and Schlegel (1996) could only point to the AGW/TID relationship. Since
75 then, data have been compiled for some parameters of medium-scale traveling ionospheric disturbances (MSTIDs), one of
76 the mechanisms for affecting the ionosphere by typhoons. The parameters of interest to typhoon/ionosphere coupling studies
77 include the propagation direction. Of particular interest to the current study, which is conducted in the area roughly to the
78 west of Japan, are data collected in Japan. Using airglow images, a clear preference for southwestward propagation has been
79 shown by Kubota et al. (2000) and Shiokawa et al. (2003), while Fukushima et al. (2012) observations made over a seven-
80 year period in Indonesia estimated the propagation direction to be within ± 30 degrees from the source directions of MSTIDs
81 in 81% of the MSTID events. Otsuka et al. (2008) investigated a relationship between nighttime MSTIDs and sporadic *E*
82 layer, another phenomenon of interest to typhoon/ionosphere coupling. Observations made in the western hemisphere are in
83 agreement with those made over the Pacific Ocean (Paulino et al., 2016; Frissell et al. 2014; Paulino et al., 2018). The latter
84 study by Paulino et al. is noteworthy because it showed that the observed anisotropy in the propagation direction can fully be
85 explained by the filtering process of the wind.

86 The results of the latest observations are presented in papers by Kong et al. (2017), Li et al. (2018), Zhao et al.
87 (2018), Song et al. (2019), Wen and Jin (2020), Chen et al. (2020), Ke et al. (2020), Zhao et al. (2020), Das et al. (2021),
88 Freeshah et al. (2021), Chernogor et al. (2021, 2022), Zakharov et al. (2019, 2022). They show that the influence of typhoons
89 on the ionosphere might be expected to significantly depend on typhoon parameters, local time, season, solar cycle changes,
90 and on the state of atmospheric and space weather. To date, there remains insufficient knowledge about this influence and
91 therefore the study of the ionospheric response to any new typhoon is of interest. In this paper, super typhoon Kong-Rey, the
92 most powerful worldwide typhoon in 2018, has been chosen to analyze the ionospheric response to the typhoon action.

93 The scientific objectives of this study is to determine the response of the ionosphere to approaching super typhoon
94 Kong-Rey by making use of variations in Doppler spectra, Doppler shift, and HF signal amplitudes recorded at oblique

95 propagation paths, as well as to estimate the parameters of the ionospheric perturbations. An estimate of the joint influence of
 96 the typhoon and the dusk terminator is also a phenomenon of interest. The observations were made using the Harbin
 97 Engineering University, the People’s Republic of China (PRC), multifrequency multiple path coherent software defined radio
 98 system for probing the ionosphere at oblique incidence. The data sets discussed in this paper may be obtained from the
 99 website at <https://dataverse.harvard.edu/dataset.xhtml?persistentId=doi:10.7910/DVN/VHY0L2> (Garmash, 2022), and the
 100 software for Passive 14-Channel Doppler Radar may be obtained from
 101 <https://dataverse.harvard.edu/dataset.xhtml?persistentId=doi:10.7910/DVN/MTGAVH> (Garmash, 2021).

102 2 General information on super typhoon Kong-Rey

103 Table 1 presents basic information on typhon Kong-Rey, a Category 5 tropical storm; part of the information was retrieved
 104 from <http://agora.ex.nii.ac.jp/digital-typhoon/summary/wnp/s/201825.html.en>. It shows that the typhoon originated on 29
 105 September 2018 and ceased to exist on 6 October 2018. A noticeable decrease in pressure took place on 30 September 2018,
 106 when the pressure reached a minimum value of 900 hPa, while the pressure deficit attained a maximum of 105 hPa (see also
 107 Figure 1). The wind speed attained a maximum of 215 km h⁻¹ or 60 m s⁻¹, with 77 m s⁻¹ maximum gusts. The largest radius
 108 of the storm wind was 260 km, and the largest radius of the gale wind was 750 km. The length of the typhoon path is
 109 estimated to be 4,107 km, with an average speed of 23.6 km h⁻¹ or 6.6 m s⁻¹. The dynamic wind pressure is estimated to
 110 attain 2.25 kPa, with a maximum gust pressure of 3.8 kPa. The kinetic energy of the rotating air was estimated to be close to
 111 1.65×10¹⁸ J, while the mean power was estimated to attain 1.7×10¹³ W. On 1 and 2 October 2018, the super typhoon energy
 112 was a maximum, and on 2 October 2018 the typhoon moved to the system probing the ionosphere closer by ~600 km (Figure
 113 1). On 5 October 2018, the typhoon was 250 km off the shores of the PRC, when the pressure deficit was observed to be
 114 ~30 hPa.

115 Table 1. Basic parameters of super typhoon Kong-Rey (Courtesy of Asanobu KITAMOTO, Digital typhoon,
 116 National institute of informatics, Japan).

Birth	2018-09-29 06:00:00 UTC
Death	2018-10-06 12:00:00 UTC
Lifetime	174 h/7.250 days
Minimum Pressure	900 hPa
Pressure Maximum Deficit	105 hPa
Maximum Wind Speed	215 km h ⁻¹ (60 m s ⁻¹)
Largest Radius of Storm Wind	260 km
Largest Radius of Gale Wind	750 km
Length of Movement	4,107 km
Average Speed	23.6 km h ⁻¹ (6.56 m s ⁻¹)

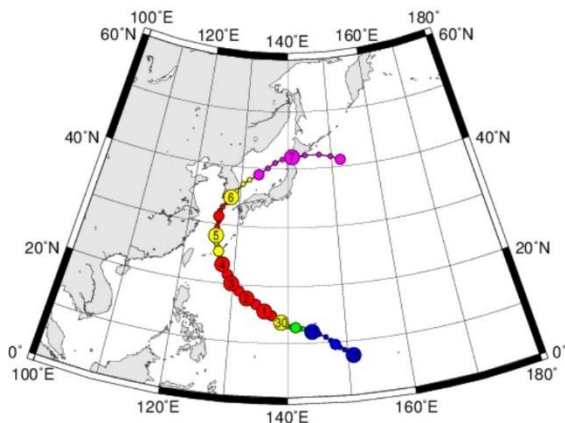
Range of Movement	Latitude 25.3°: Longitude 16.7°
Typhoon Kinetic Energy	1.65×10^{18} J
Typhoon Power	1.7×10^{13} W
Rainfall	250–300 mm h ⁻¹
Maximum Pressure Drop	–25 hPa / 6 h; –40 hPa / 12 h –65 hPa / 24 h; –96 hPa / 48 h
Data Start	2018-09-28 00:00:00 UTC
Data End	2018-10-07 12:00:00 UTC
Data Duration	228 h / 9.500 days

117 3 Analysis of the state of space weather

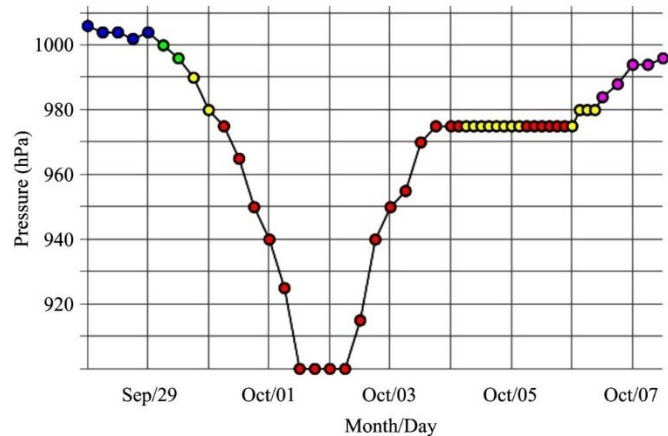
118 A comprehensive analysis of space weather is required in order to ascertain the ionospheric response to the super typhoon
119 action.

120 Figure 2 accumulates knowledge regarding the state of space weather during the super typhoon Kong-Rey event.
121 First, consider the parameters of the solar wind (retrieved from <https://omniweb.gsfc.nasa.gov/form/dx1.html>). Under quiet
122 conditions, the proton number density is observed to be close to 5×10^6 m⁻³, whereas on 29 September 2018 and 1, 3, and 5
123 October 2018, it shows increases up to $(15-20) \times 10^6$ m⁻³. On 26 and 30 September 2018, as well as on 3–4 October 2018, the
124 plasma flow speed increases from ~ 400 km s⁻¹ to 500–520 km s⁻¹. During the same UT period, plasma temperature increases
125 from $\sim (2-3) \times 10^4$ K to $\sim (1.2-1.5) \times 10^5$ K, while the dynamic solar wind pressure increases from ~ 1 nPa to 4–5 nPa. The B_y
126 component of the interplanetary magnetic field exhibits temporal variability within the –5.9 nT to 11.6 nT limits, while the
127 B_z component changes from –4.7 nT to 4.0 nT.

a



b



128

129 **Figure 1: Super typhoon Kong-Rey (a) trajectory and (b) pressure (Courtesy of Asanobu KITAMOTO, Digital Typhoon, National**
130 **Institute of Informatics, Japan).**

131 On 26 and 29 September 2018, as well as on 1 and 3–4 October 2018, the calculated energy input, ϵ_A , into the
132 Earth's magnetosphere from the solar wind shows increases up to $\sim 5 \text{ GJ s}^{-1}$.

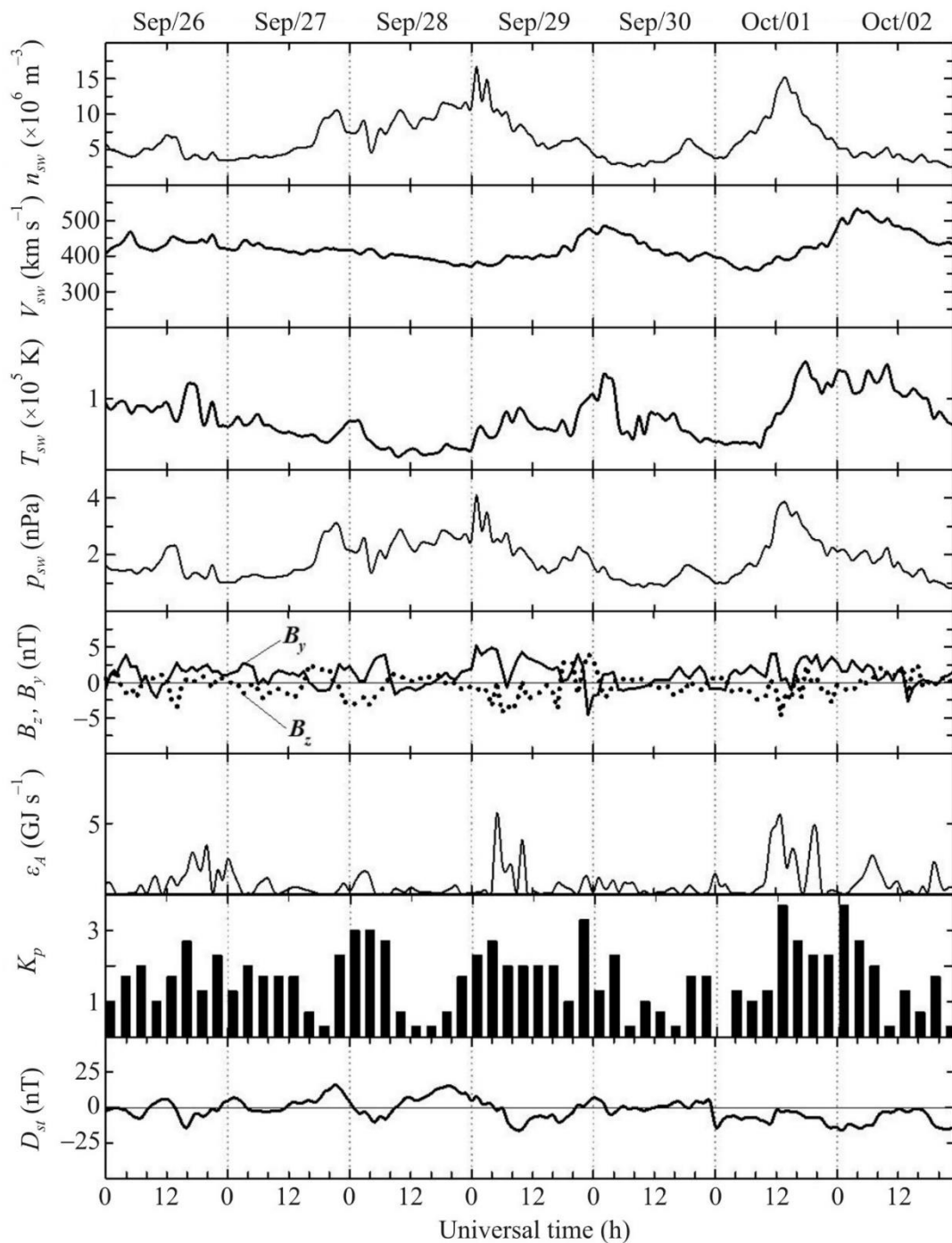
133 The K_p index exhibits sporadic increases to 3.0–3.7, while the D_{st} index shows fluctuations from -16 nT to
134 16 nT .

135 Table 2 presents temporal variations in the radio flux at 10.7 cm ($F_{10.7}$) index for the 26 September to 09 October
136 2018 period.

137 Thus, solar activity and the state of space weather were conducive to observing the ionospheric effects from typhoon
138 Kong-Rey. Only on 7 October 2018, a moderate magnetic storm started, with $K_{p\text{max}} = 5.3$, and $D_{st\text{min}} \approx -53 \text{ nT}$. Thus, the days
139 of 26 and 27 September 2018, the first half of 28 and entire 29 September 2018, and partially the days of 1 and 2 October
140 2018 were weakly disturbed. The magnetic storm occurred after the typhoon ceased to exist, from October 7 through 9,
141 2018, when the Doppler shifts exhibited variations greater than those observed under the action of the typhoon, which
142 justifies the need for a thorough analysis of space weather. Consequently, 28 September 2018, and 4 October 2018, have
143 been chosen to be quiet time references.

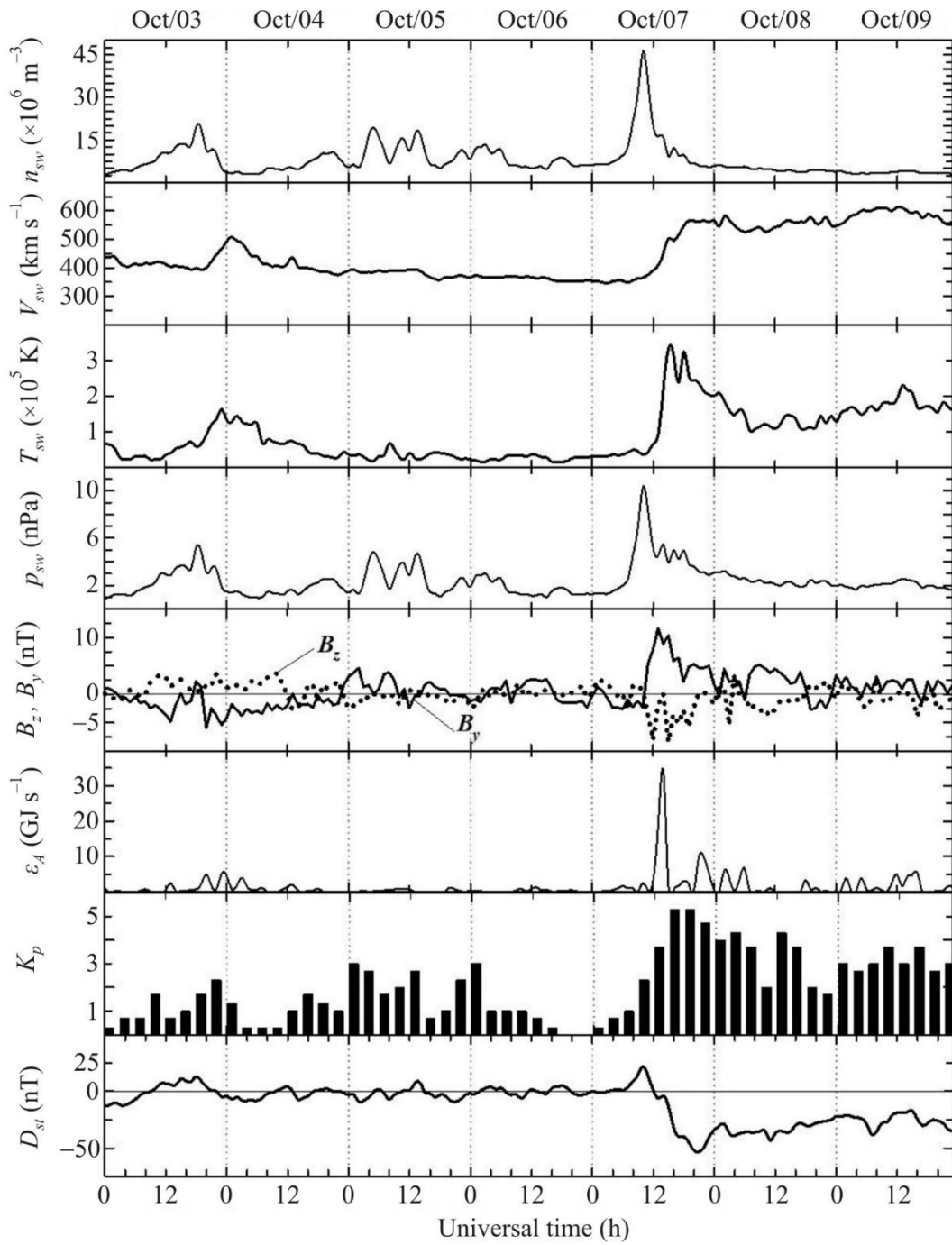
144 **4 Analysis of the state of the ionosphere**

145 The state of the ionosphere was monitored by the ionosonde nearest to Harbin, i.e., the WK546 URSI code ionosonde
146 located in the city of Wakkanai (45.16°N , 141.75°E) in Japan (Guo et al., 2019a, 2019b, 2020; Chernogor et al., 2020; Luo
147 et al., 2020). Figure 3 shows UT variations in the main ionogram parameters. The minimum frequency, f_{min} , observed on
148 ionograms exhibited fluctuations around 1.5 MHz . The critical frequencies of the E layer, f_{oE} , were close to 3 MHz during
149 the day, and gradually decreased to $1.8\text{--}2.0 \text{ MHz}$ in the evening hours. At night, measurements of f_{oE} were impossible. The
150 blanketing frequency of the sporadic E layer, most often, showed fluctuations within the $3\text{--}8 \text{ MHz}$ limits, however
151 sometimes it could attain $13\text{--}15 \text{ MHz}$. The ordinary-wave critical frequency f_oF_2 was observed to be $4\text{--}6 \text{ MHz}$ during the
152 day and to decrease to $3.0\text{--}3.5 \text{ MHz}$ at night.



153

154 **Figure 2: Universal time dependences of the solar wind parameters: proton number density n_{sw} , plasma flow speed V_{sw} , plasma**
 155 **temperature T_{sw} , dynamic solar wind pressure p_{sw} , B_z and B_y components of the interplanetary magnetic field, calculated energy**
 156 **input, ϵ_A , into the Earth's magnetosphere from the solar wind; and K_p - and D_{st} -indices for the 26 September–2 October, 2018**
 157 **period.**

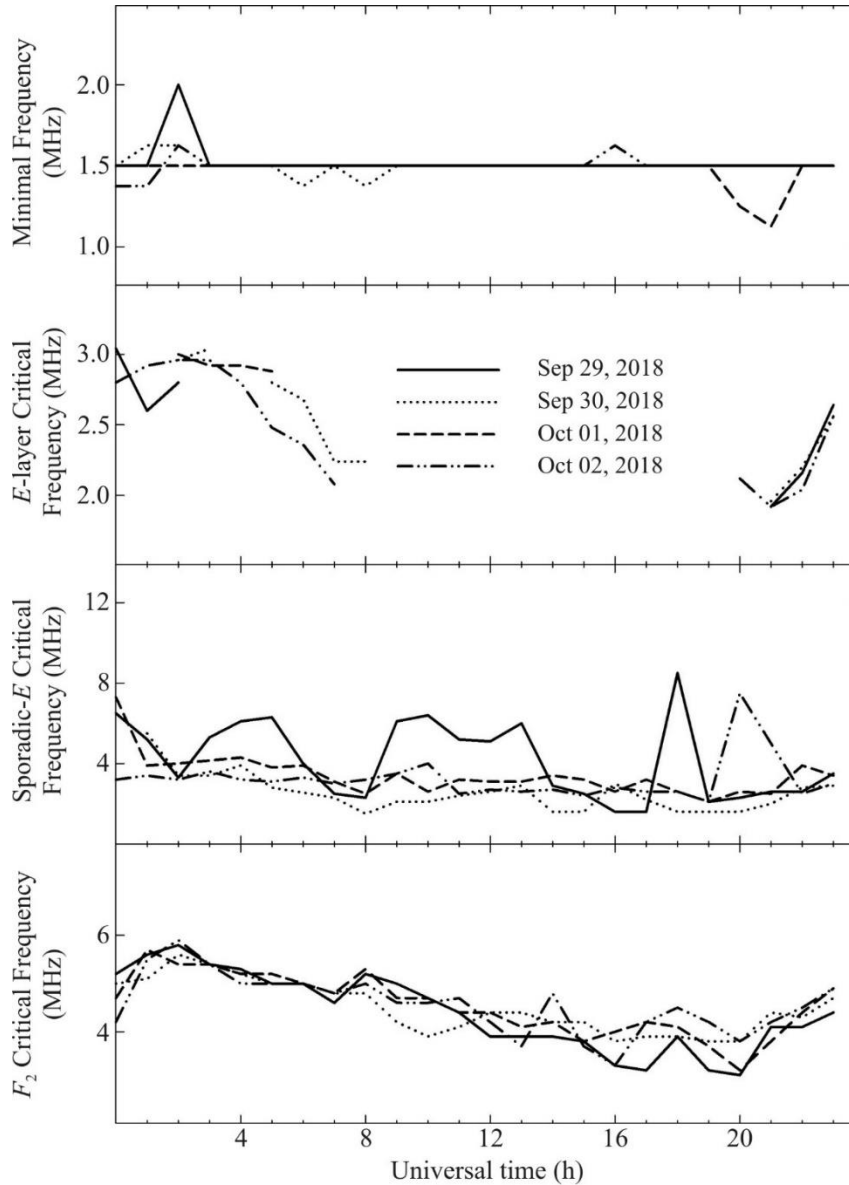


158
 159
 160
 161
 162
 163

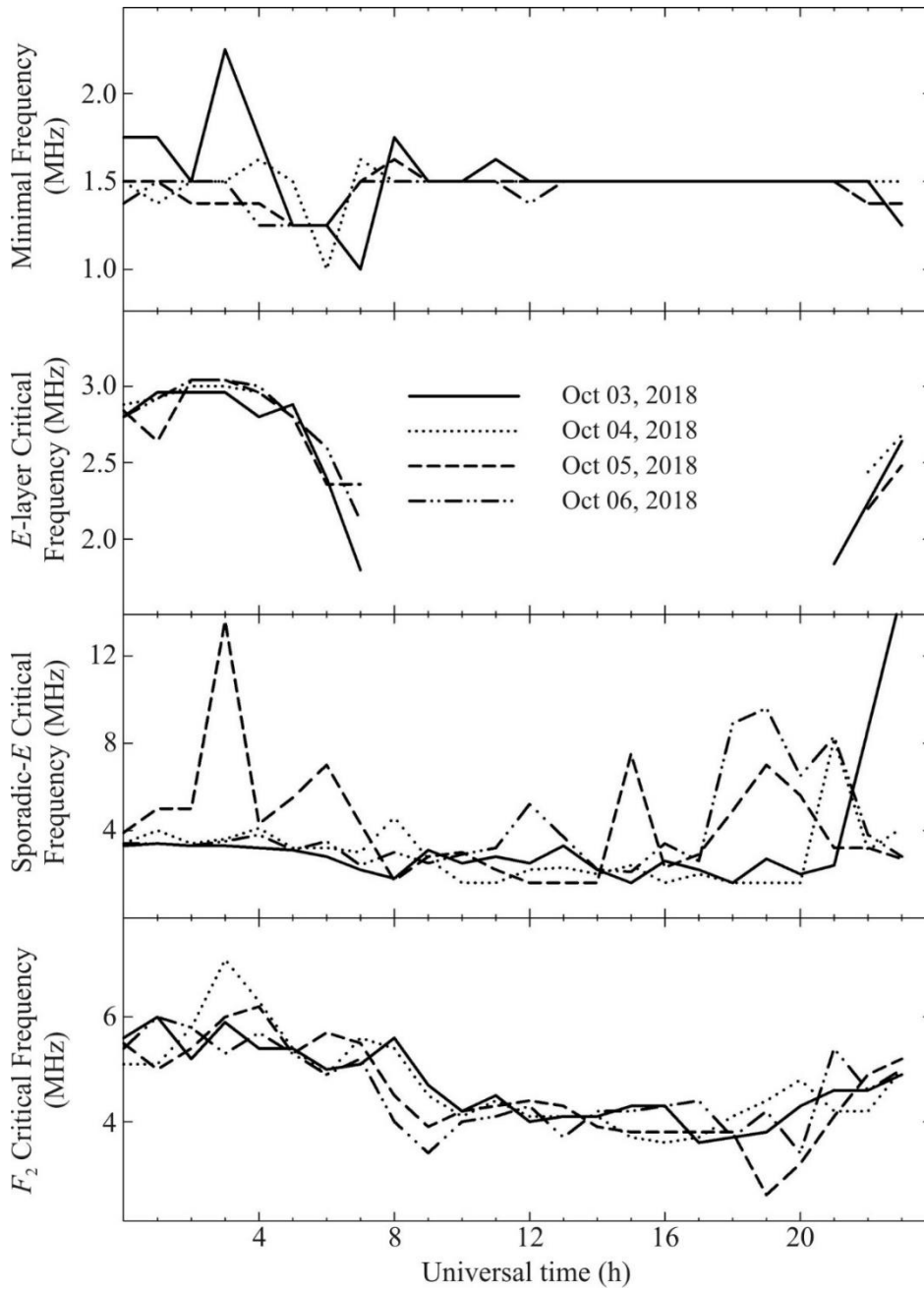
Figure 2: Continued for the 03–09 October 2018 period.

Table 2. Daily $F_{10.7}$ index for the 26 September 2018–9 October 2018 period

Date (2018)	26 Sep.	27 Sep.	28 Sep.	29 Sep.	30 Sep.	1 Oct.	2 Oct.	3 Oct.	4 Oct.	5 Oct.	6 Oct.	7 Oct.	8 Oct.	9 Oct.
$F_{10.7}$	69.3	67.4	69.4	68.9	68.5	70.3	67.1	68.4	67.2	68.7	68.6	69.4	68.7	69.3



168 **Figure 3: Universal time variations in ionogram parameters determined with an update rate of one measurement per 1 h: critical**
 169 **frequencies f_{\min} , f_oE , f_oE_s , and f_oF_2 for the 29 September–2 October 2018 period.**



170
171
172

Figure 3: Continued for the 3–6 October 2018 period.

173
174
175
176

Figure 4 shows temporal variations in the virtual heights. The virtual heights h'_E are observed to vary mainly within the 95–105 km, whereas the virtual heights h'_{Es} most frequently show variations within the 90–110 km limits, which could sometimes exhibit an increase to 140–160 km.

177 5 Instrumentation and techniques

178 The study of the effects from the super typhoon was conducted using the Harbin Engineering University multifrequency
179 multiple path coherent software defined radio system for probing the ionosphere at oblique incidence (Guo et al., 2019a,
180 2019b, 2020; Chernogor et al., 2020; Luo et al., 2020). The system utilizes radio transmissions of broadcast stations located
181 in the PRC, the Republic of Korea, Japan, the Russian Federation, and Mongolia, the signals of which are received and
182 processed at the Harbin Engineering University campus (45.78°N, 126.68°E).

183 Continuous monitoring of the dynamic processes operating in the ionosphere is done along 14 propagation paths in
184 the ~5 – 10 MHz band (Table 3, Figure 5) as described by Guo et al. (2019a, 2019b, 2020), Chernogor et al. (2020), and Luo
185 et al. (2020). In the event under study, post-analysis of the data acquired along six propagation paths has shown that the data
186 are not suitable for processing.

187 Monitoring the dynamic processes in the ionosphere is done via calculating the temporal dependences of the
188 Doppler spectra and signal amplitudes. The Doppler spectra are used to plot the Doppler shift as a function of time, $f_D(t)$, for
189 all rays under analysis.

190 Spectrum analysis is performed applying the autoregressive technique of Marple (1987), which provides a
191 frequency resolution of 0.01 Hz over ~20 s intervals with 7.5 s time resolution.

192 The $f_D(t)$ dependences can be used to calculate the trend $\bar{f}_D(t)$, the fluctuations $\delta f_D(t) = f_D(t) - \bar{f}_D(t)$, and the
193 systems spectral analysis can be undertaken over 60 – 280 min intervals to select harmonics in the $T \leq 5$ min and $T = 10 -$
194 140 min period ranges (Chernogor, 2008).

195 For over about 50 years, one of the co-authors, Chernogor, L. F., has developed a general methodology for revealing
196 perturbations launched in the ionosphere by various significant inputs of energy into the lithosphere–atmosphere–
197 ionosphere–magnetosphere system. To put the development of this methodology into perspective, one should remember that
198 the development of this methodology has been accompanied by tremendous, unparalleled technological advances, from
199 analogue instruments and film-based recordings to new software-defined radio sensors.

200 Used in this study, the radio system probes the ionosphere at 14 radio propagation path midpoints of the order of
201 1,000 km distance apart, which are randomly distributed in the ~100–300 km altitude range. Generally, the perturbations
202 under study may be produced either by an impulsive release of energy at a fixed location, as in the case of an earthquake, or
203 by significant releases of energy, which change their location and power as well as persist for a few days, as in the case of a
204 typhoon. On the way from their origin to the radio propagation path midpoints in the upper atmosphere, the perturbations
205 may undergo various nonlinear transformations. In the case of a typhoon event, atmospheric gravity waves, generated via a
206 nonlinear process (Drobnyazko and Krasil'nikov, 1975), travel up to the ionosphere (partially dissipating their energy for
207 heating the neutral air) and launch secondary gravity waves in the wave breaking regions (see, e.g., Vadas et al., 2003; Vadas
208 and Crowley, 2010). The latter waves in the atmosphere modulate the electron density, which can result in the level of
209 reflection variability, the appearance of a few rays, or in some cases, in diffuseness in the Doppler measurements or spread F

210 in ionograms, which is an indicator of the occurrence of plasma irregularities in the ionosphere (see, e.g., Perkins (1973)). As
211 a consequence, the measurements taken at each midpoint produce a single realization of a random process, which means that
212 the Doppler or amplitude signatures of the sources of perturbations are unrepeatably neither in time nor in space. The
213 observational methodology that enables identification and investigation of such perturbations arising from any deposition of
214 large amounts of energy include the following basic principles invoked consecutively. (i) During the initial stage of
215 employing this methodology, the perturbations originating from a particular powerful source are in principle not
216 distinguishable qualitatively from the perturbations caused by energy released from any other powerful source. (ii) A
217 particular powerful source releasing energy can be associated with any changes in the character of the signal (Doppler shift,
218 Doppler spectrum, the number of rays, discrete spectrum broadening, changes in the signal amplitude, etc.), in accordance
219 with (i) above). This condition is necessary but insufficient. (iii) Intercomparisons between the behavior of radio wave
220 characteristics observed prior to and after an impulsive release of energy must be made. (iv) An intercomparison of the
221 behavior of the radio wave characteristics observed on the day when a particular massive release of energy occurred and
222 during quiet time reference days must be made. Any differences may be due to this particular source. Points (iii) and (iv)
223 serve as control stages. During these stages, the effects that are not associated with the massive release of energy are
224 discarded. (v) The magnitudes of the speeds of propagation of the disturbances must have a physical significance and
225 correspond to known types of waves (seismic, atmospheric gravity waves, infrasound, magnetohydrodynamic). This stage
226 proves sufficiency. (vi) The data acquired over a large (10–14, in the case of the Harbin Engineering University system)
227 number of propagation paths must be consistent with each other to prove sufficiency additionally. (vii) The main signs of a
228 particular powerful source should be observed during other analogous events. First of all, this principle refers to the observed
229 velocities and types of waves. The speeds of perturbations traveling to the radio propagation path midpoints should be
230 contained within the speed limits characteristic of each particular wave type.

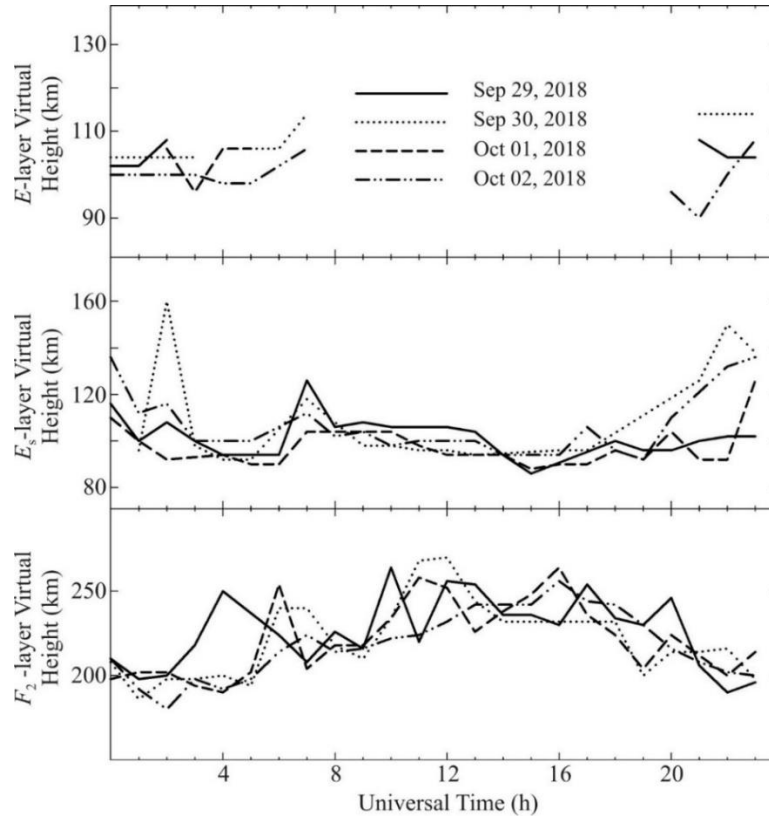
231 **6 Ionospheric results from oblique incidence sounding**

232 The post analysis of the data collected during the super typhoon Kong-Rey event has shown that the transmissions from only
233 eight of the fourteen transmitters in the ~6–10 MHz band are suitable for studying the super typhoon Kong-Rey event
234 (Figure 5). The specifications of the transmitters and radio-wave propagation paths are presented in Table 3. Since the
235 lengths of the propagation paths are found to be ~1000–2000 km and the frequencies of the sounding radio waves are
236 relatively small, the sounding waves were reflected either from the *E* layer or from the sporadic *E* during the daytime when
237 the Doppler shift, f_D , was observed to be ~0 Hz. Consequently, these measurements were ineffective in observing
238 ionospheric dynamics. At night, the radio waves were reflected from the ionospheric *F* region and only sometimes from the
239 sporadic *E*. The Doppler shift of the radio waves reflected from the *F* region exhibited variations from ~0.1 Hz to ~0.5 Hz
240 and greater. Therefore, the measurements made during nights, evenings, and mornings could be used for studying

241 ionospheric dynamics. The observations suffer another drawback: the transmitters of the broadcast radio stations did not
 242 transmit continuously.

243 The Doppler spectra, Doppler shift, and the signal amplitudes in the main rays along all propagation paths exhibited
 244 relatively small variability. The smallest variations were observed to occur on 28 September 2018, which was chosen to be
 245 as a quiet time reference.

246 The Doppler spectra and Doppler shift in the main rays, and the signal amplitudes showed the greatest variability on 7
 247 and 8 October 2018 because it occurred due to the magnetic storm, which is not dealt with in detail in this study.

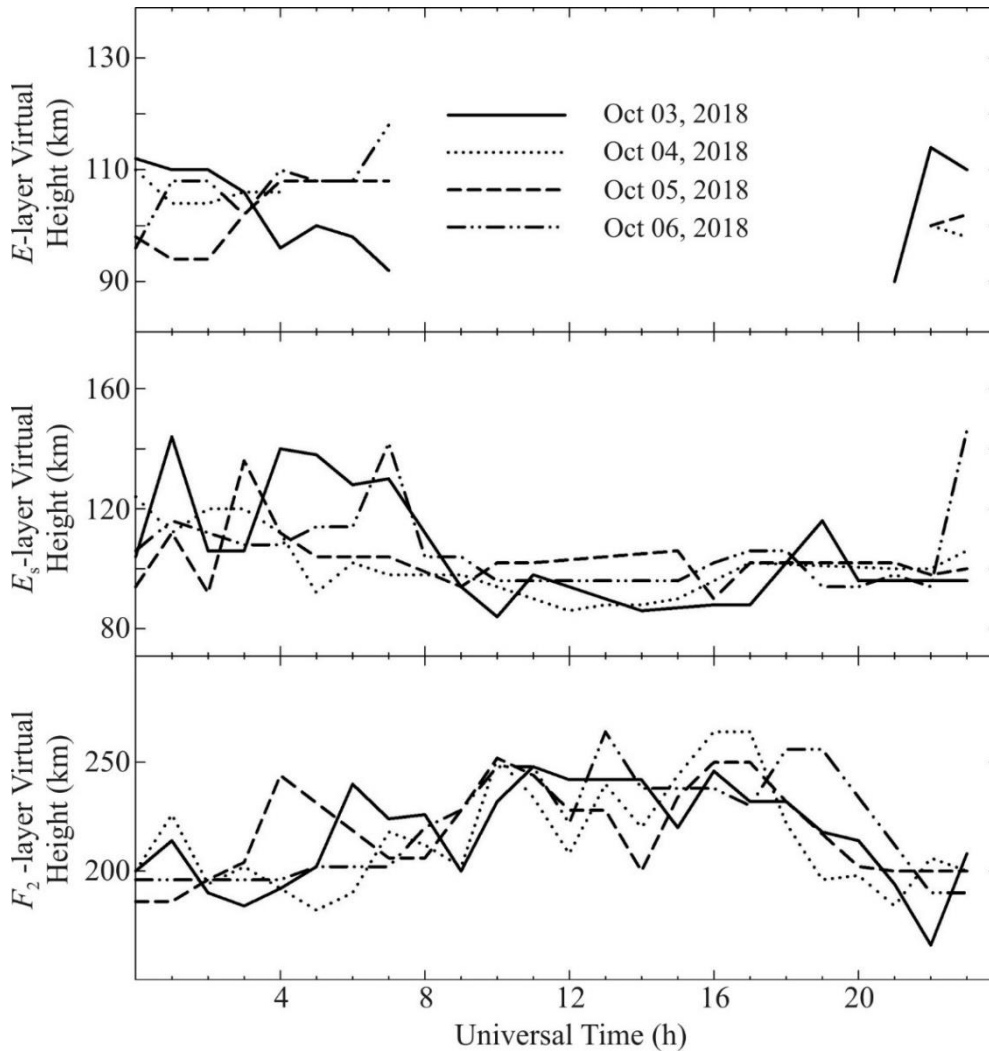


248
 249 **Figure 4: Universal time variations in ionogram parameters determined with an update rate of one measurement per 1 h: virtual**
 250 **heights h'_E , h'_{Es} , and h'_{F2} for 29 September–2 October 2018 period.**

251 6.1 Hwaseong to Harbin radio-wave propagation path

252 This transmitter operating at 6,015 kHz is located in the Republic of Korea at a great-circle range, R , of ~ 950 km from the
 253 receiver; it was switched off from 00:00 UT to 03:30 UT.

254 On 29 and 30 September 2018, the Doppler shift was observed to be less than $\pm(0.2\text{--}0.3)$ Hz (Figure 6). From 09:00
 255 UT to 15:00 UT, the Doppler spectra showed diffuseness, and the Doppler shift exhibited quasi-sinusoidal variations with a
 256 $\sim 20\text{--}30$ min period, T , and a $\sim 0.1\text{--}0.2$ Hz amplitude, f_{Da} , respectively.



257
258
259
260

Figure 4: Continued for the 2–6 October 2018 period.

261
262

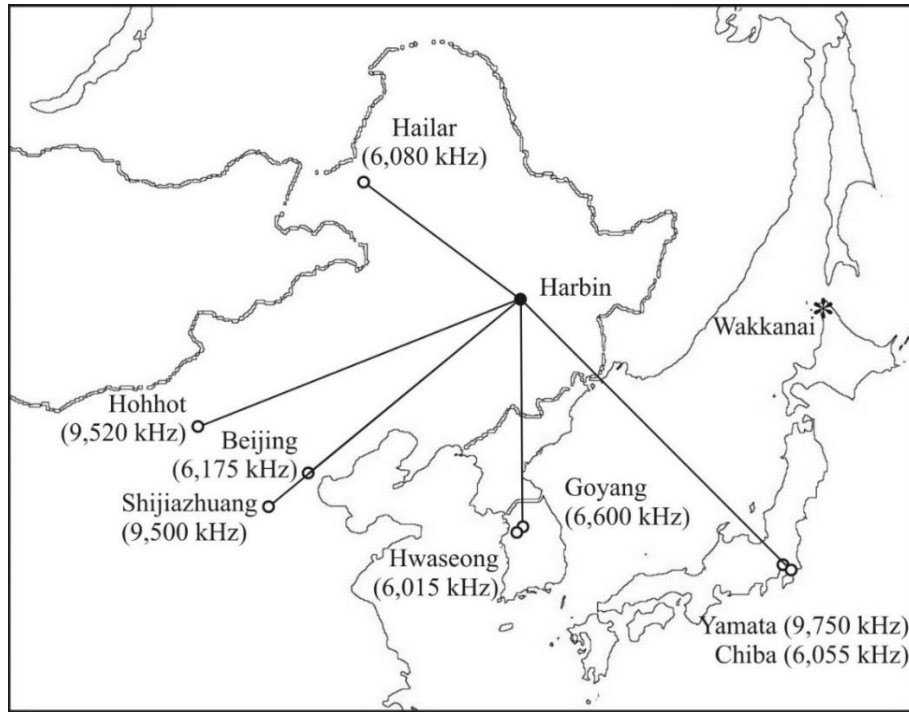
Doppler spectra broadening was absent during the interval from 1 to 6 October 2018. On 1 October 2018, $f_{Da} \approx 0.3$ – 0.5 Hz, and $T \approx 20$ – 120 min.

263
264
265
266
267

On 2 October 2018, the 20–80 min period amplitude of Doppler shift did not exceed 0.1–0.3 Hz. A single 140 min period wavelet in f_{Da} up to 0.5 Hz originated on 3 October 2018. On 4 October 2018, the amplitude of Doppler shift did not exceed 0.2 Hz, while observable quasi-sinusoidal processes were practically absent. On 5 and 6 October 2018, the Doppler shift exhibited sporadic increases up to 0.5–0.6 Hz and decreases down to $-(0.5$ – $0.7)$ Hz; over the rest of the time, $f_{Da} \approx 0.1$ Hz, while $T \approx 20$ – 30 min.

268

The amplitudes of individual variations in the signal strengths did not exceed 10–15 dBV.



270

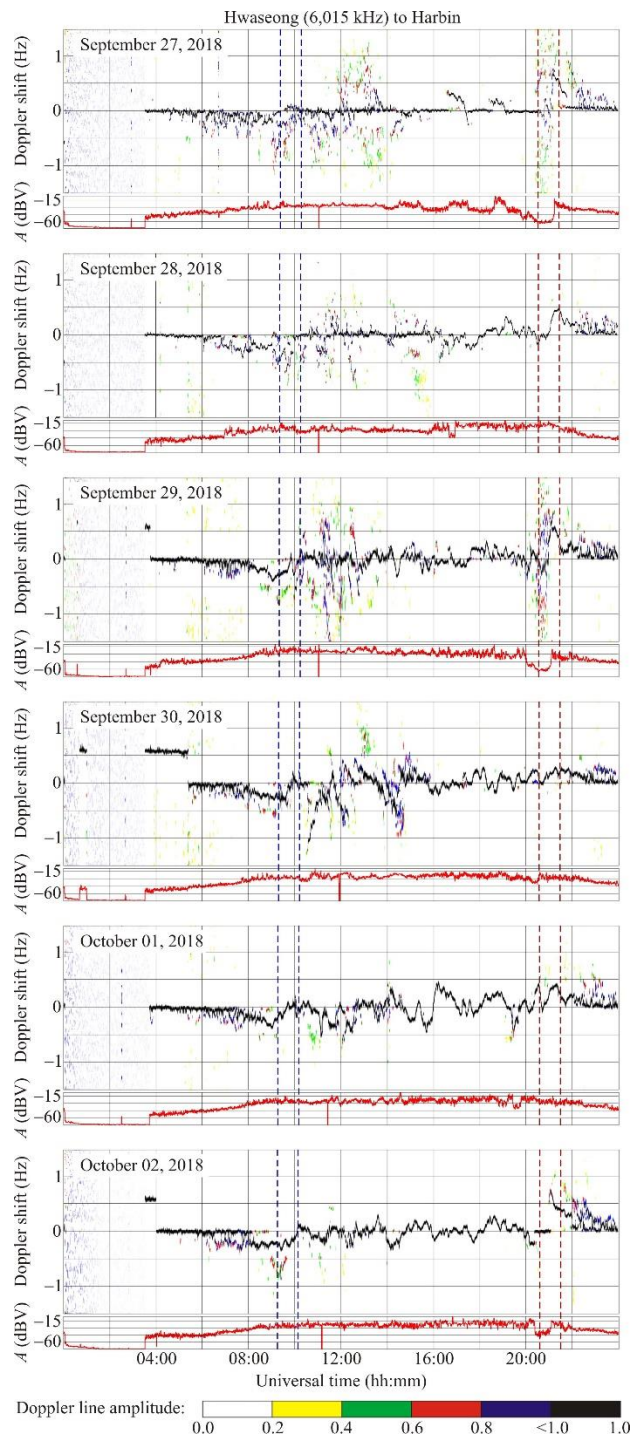
271 **Figure 5: Layout of the propagation paths used for monitoring dynamic processes operating in the ionosphere.**

272

273

Table 3. Basic information on radio-wave paths. The data are retrieved from <https://fmscan.org/index.php>.

Frequency (kHz)	Transmitter coordinates	Location (Country)	Distance to Harbin (km)	Path midpoint coordinates
6,015	37.21°N, 126.78°E	Hwaseong (Korea)	950	41.50°N, 126.73°E
6,055	35.47°N, 140.21°E	Chiba/Nagara (Japan)	1,610	40.63°N, 133.45°E
6,080	49.18°N, 119.72°E	Hailar/Nanmen (PRC)	645	47.48°N, 123.2°E
6,175	39.75°N, 116.81°E	Beijing (PRC)	1,050	42.77°N, 121.75°E
6,600	37.60°N, 126.85°E	Goyang (Korea)	910	41.69°N, 126.77°E
9,500	38.47°N, 114.13°E	Shijiazhuang (PRC)	1,310	42.13°N, 120.41°E
9,520	40.72°N, 111.55°E	Hohhot (PRC)	1,340	43.25°N, 119.12°E
9,750	36.17°N, 139.82°E	Yamata (Japan)	1,570	40.98°N, 133.25°E



274

275 **Figure 6: Universal time variations in the Doppler spectra and relative signal amplitude, A , along the Hwaseong to Harbin**
 276 **propagation path for the 27 September – 2 October 2018 period. Vertical dashed lines designate instances of sunrise (two right red**
 277 **lines) and sunset (two left blue lines) at the ground and at 100 km altitude. The signal amplitude, A , at the receiver output in**
 278 **decibels, dBV (relative to 1 V), is shown below the Doppler spectra in each panel.**

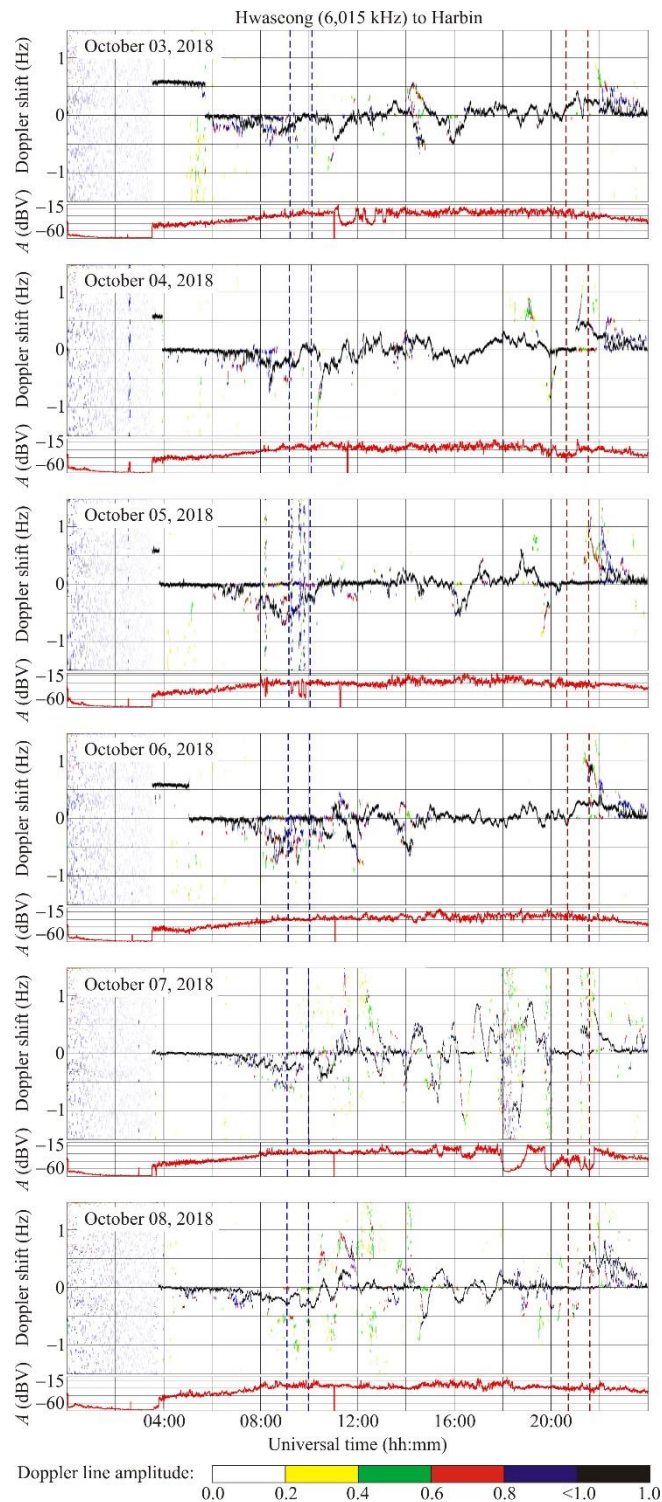


Figure 6: Continued for the 3–8 October 2018 period.

281 **6.2 Chiba/Nagara to Harbin radio-wave propagation path**

282 The radio station operating at 6,055 kHz is located in Japan at a great-circle range, R , of $\sim 1,610$ km; it was switched off from
283 15:00 UT to 22:00 UT.

284 Figure 7 shows that the Doppler spectra exhibit significant, up to ± 1.5 Hz, broadening and such a diffuseness that
285 the main ray is practically not distinguishable during the 27–30 September 2018 period. On 1 October 2018, the Doppler
286 shift shows ~ 60 min period, T , quasi-sinusoidal variations with an ~ 0.3 – 0.4 Hz amplitude, whereas the signal amplitude,
287 $A(t)$, exhibits ~ 30 min period, T , variations with a 5 dBV amplitude. On 5 and 6 October 2018, quasi-sinusoidal variations
288 are also noted in the Doppler spectra, with ~ 0.4 – 0.6 Hz amplitudes, f_{Da} , and with ~ 60 min and 120 min periods, T . On 6
289 October 2018, the signal amplitude exhibits ~ 30 min and ~ 60 min period, T , quasi-sinusoidal variations with a ~ 5 dBV
290 amplitude.

291 **6.3 Hailar to Harbin radio-wave propagation path**

292 This transmitter operating at 6,080 kHz is located in the PRC at a great-circle range, R , of 646 km; the transmissions were
293 absent from 02:30 UT to 09:30 UT, whereas the observations of ionospheric dynamics were made impossible during the
294 14:30–20:00 UT period.

295 The variations in the Doppler spectra and the Doppler shift during sunlit hours on the reference days and on 1–2
296 October 2018 and 5 October 2017 were practically the same (Figure 8).

297 **6.4 Beijing to Harbin radio-wave propagation path**

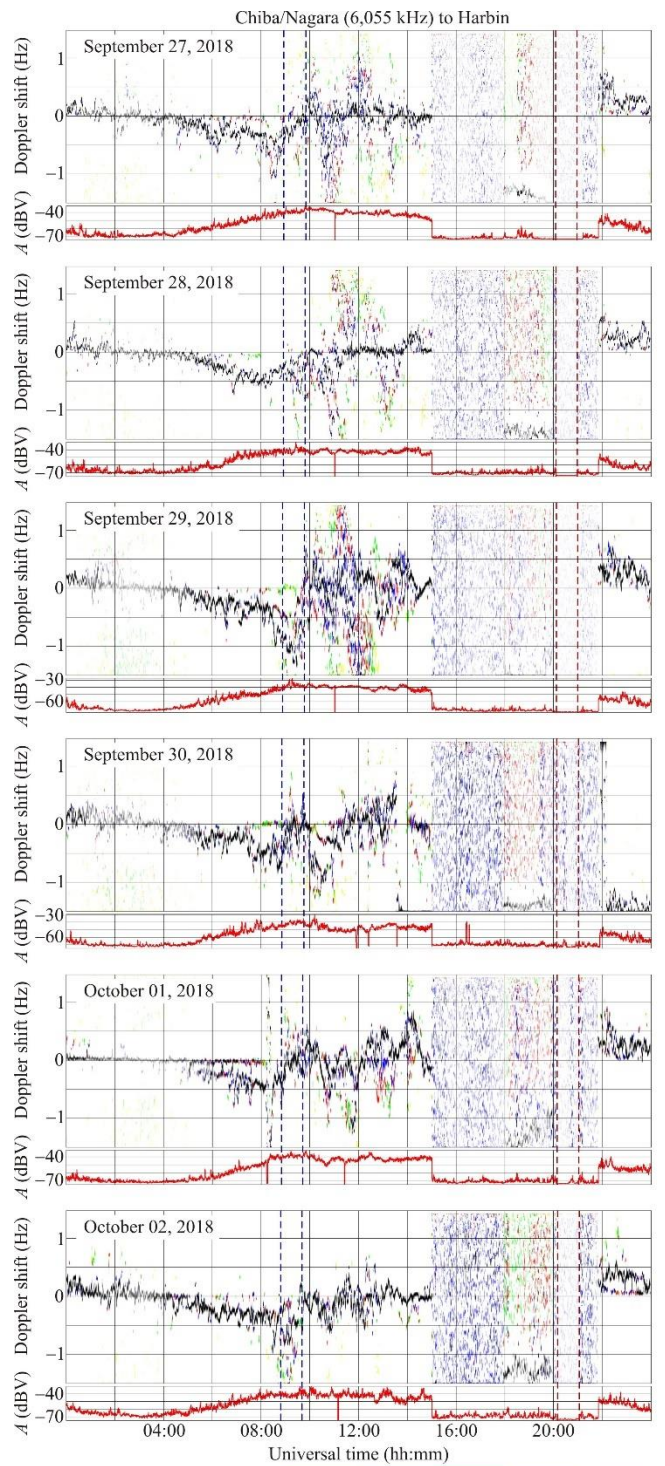
298 This radio station operated at 6,175 kHz in the PRC at a great-circle range, R , of $\sim 1,050$ km from the receiver. The
299 transmitter was switched off during 00:00 UT to 09:00 UT and from 18:00 UT to 20:00 UT periods.

300 On 29 September 2018, as well as on the next day, the Doppler shift showed small variations ~ 0.1 Hz (Figure 9),
301 which exhibited increases of up to 0.3–0.5 Hz only over separate time intervals. On 1 October 2018, the Doppler shift
302 exhibited quite ordered variations, with ~ 30 min and ~ 110 min period, T , oscillations, and amplitudes, f_{Da} , attaining 0.5 Hz.
303 On 2 October 2018, the amplitude f_{Da} decreased to 0.3 Hz, whereas the periods were observed to vary from 20 min to 110
304 min.

305 On 3, 4, and 6 October 2018, the Doppler shift showed quasi-sinusoidal variations with periods, T , in the 20 min to
306 90 min range and with 0.1–0.2 Hz amplitudes, f_{Da} .

307 After 14:00 UT on 5 October 2018, the Doppler shift amplitude, f_{Da} , was observed to increase to 0.2–0.4 Hz and to
308 exhibit periods, T , in the range from 20 min to 80 min.

309 The signal amplitude exhibited temporal variability within the 10 dBV limits.



Doppler line amplitude:

0.0 0.2 0.4 0.6 0.8 <1.0 1.0

310
 311 **Figure 7: The same as in Figure 6 but for the Chiba/Nagara to Harbin radio-wave propagation path at 6,055 kHz for the 27**
 312 **September – 2 October 2018 period.**

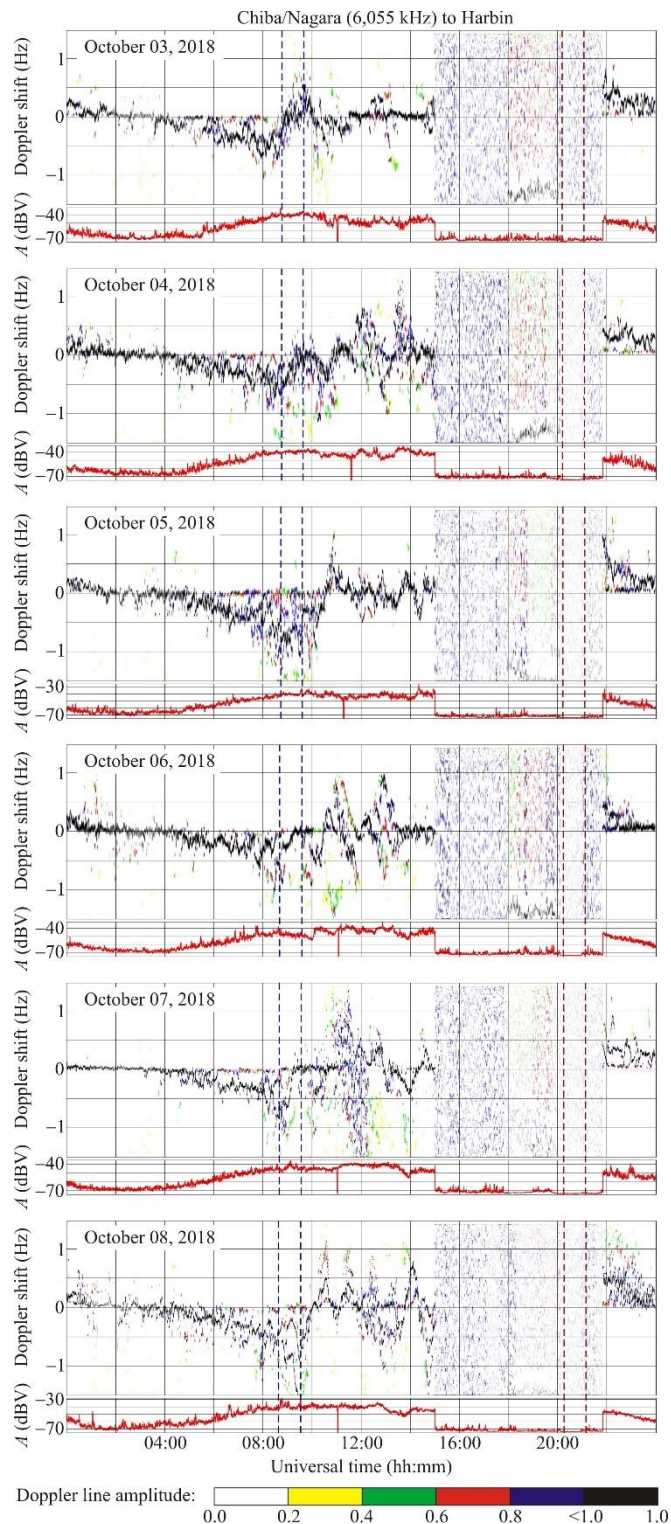
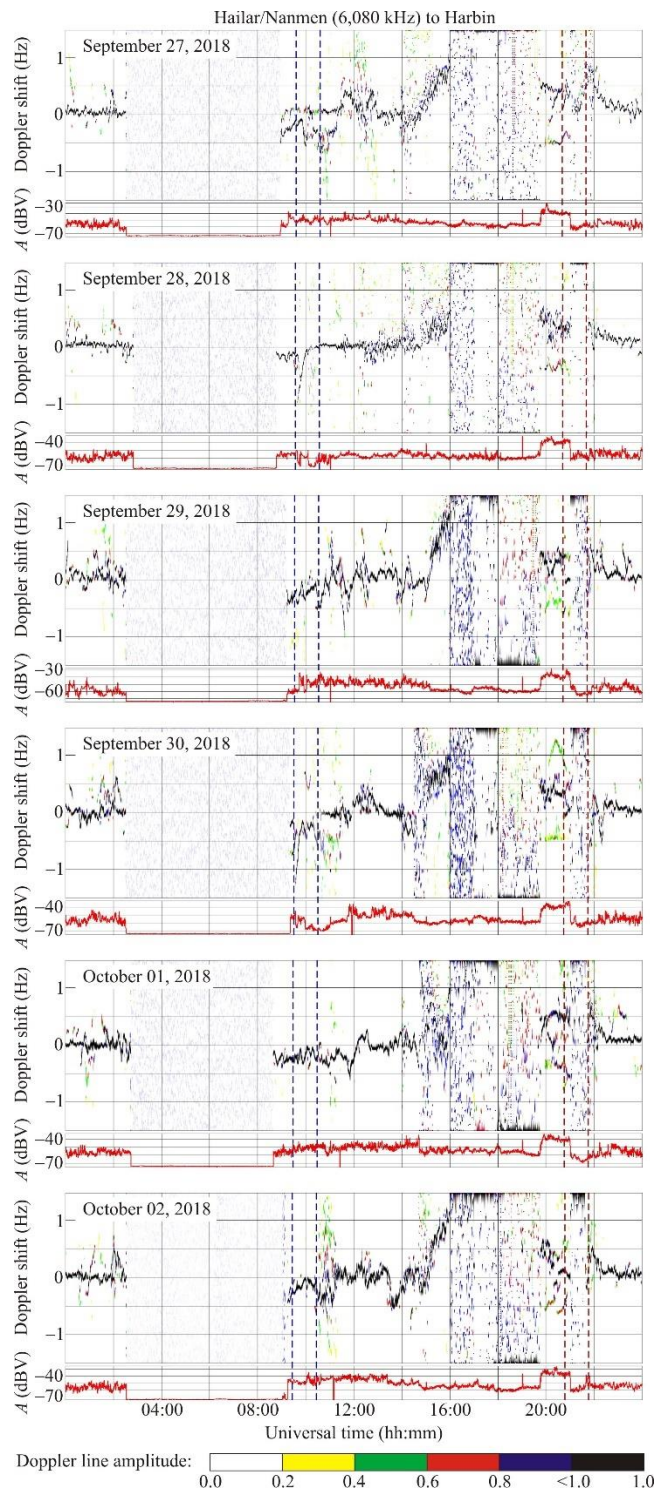


Figure 7: Continued for the 3–8 October 2018 period.



315
316
317

Figure 8: The same as in Figure 6 but for the Hailar to Harbin radio-wave propagation path at 6,080 kHz for the 27 September – 2 October 2018 period.

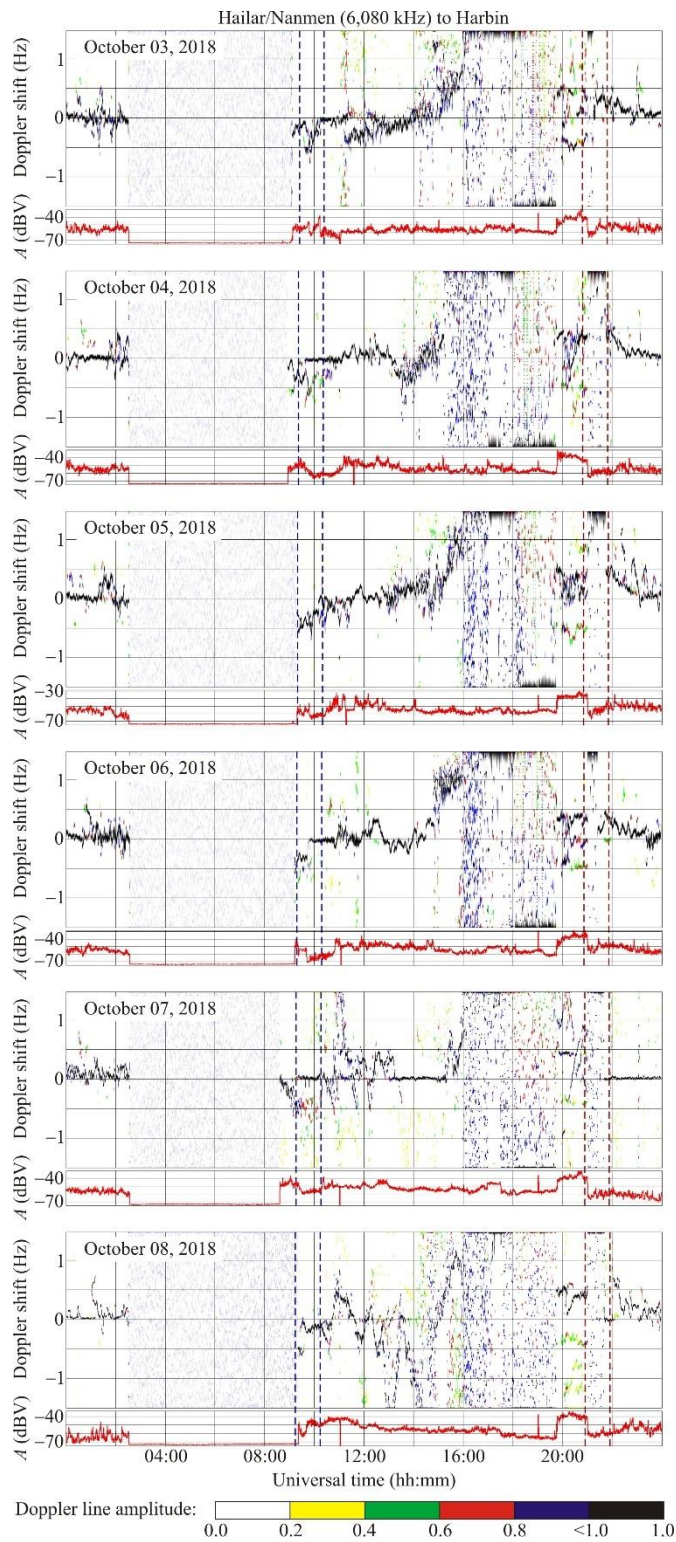
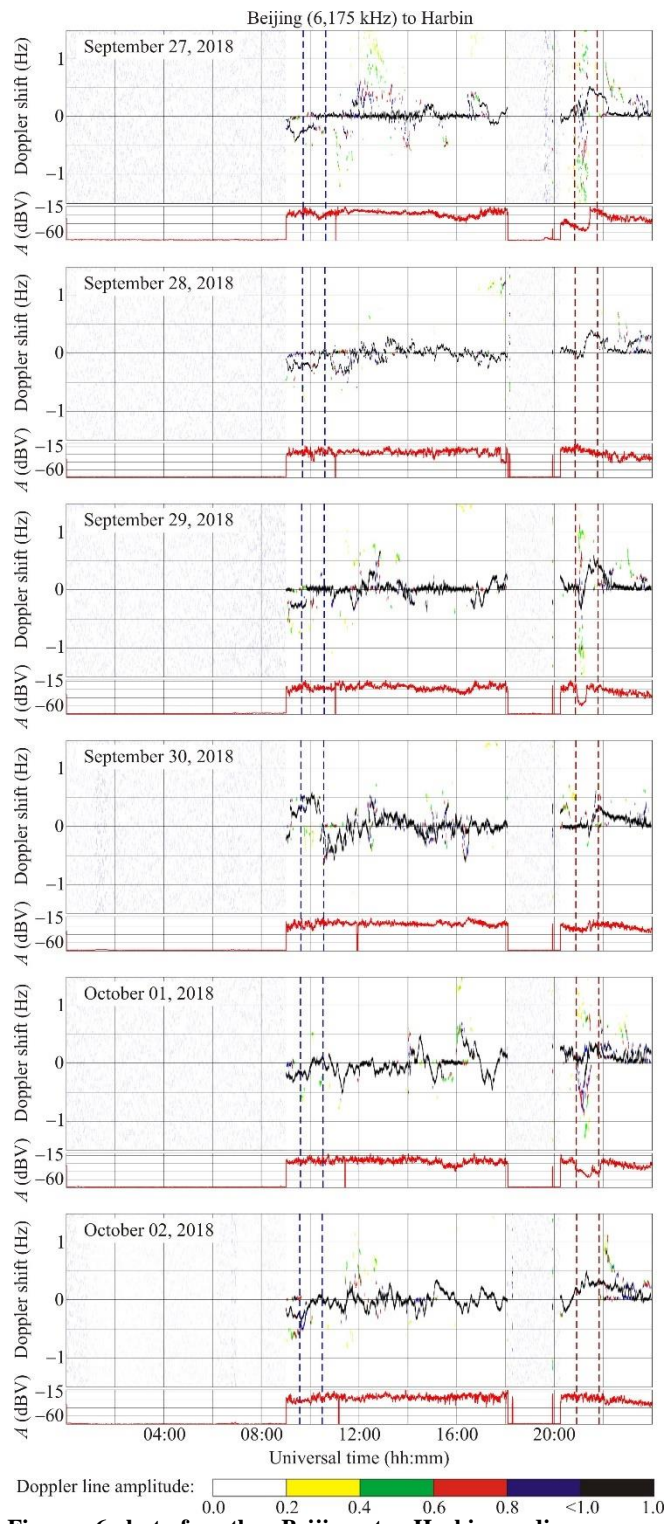


Figure 8: Continued for the 3–8 October 2018 period.



320
 321 **Figure 9: The same as in Figure 6 but for the Beijing to Harbin radio-wave propagation path at 6,175 kHz**
 322 **for the 27 September – 2 October 2018 period.**

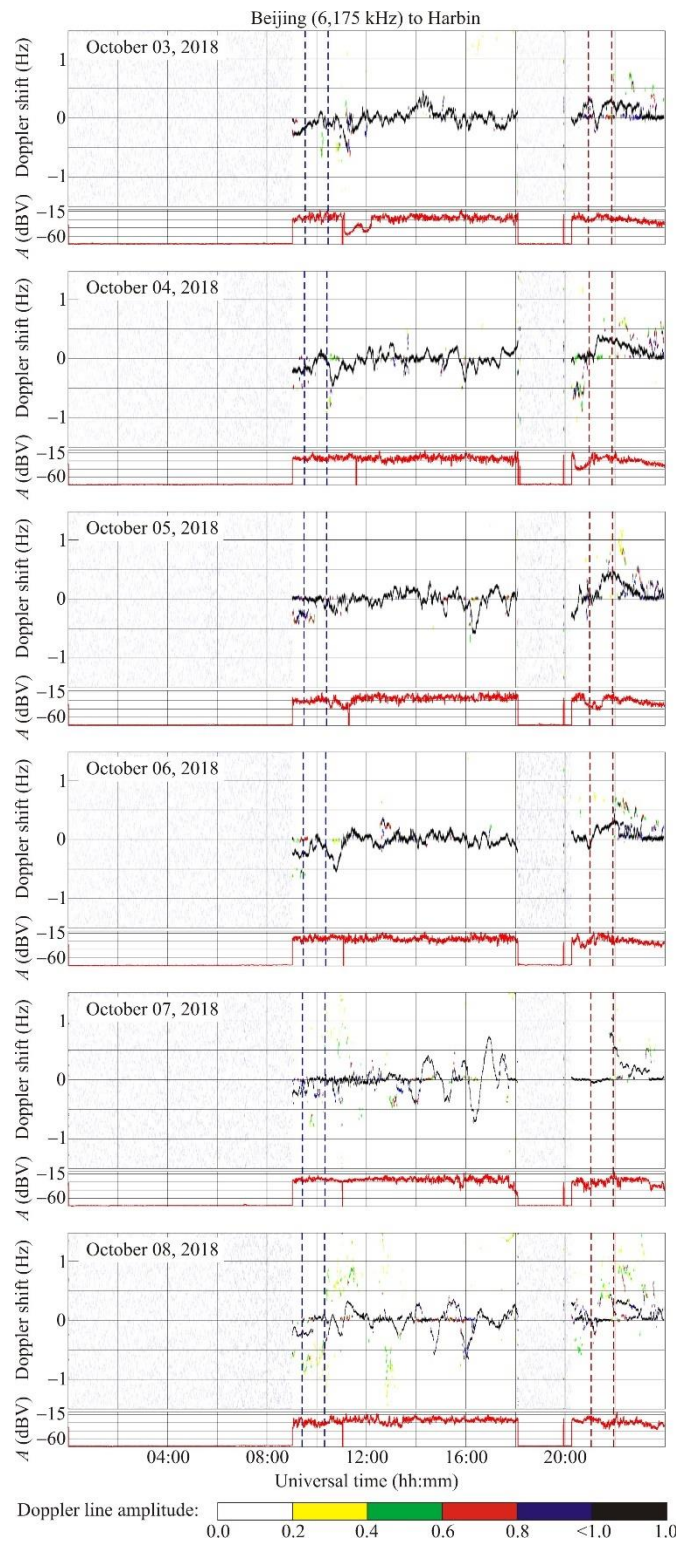


Figure 9: Continued for the 3–8 October 2018 period.

325 **6.5 Goyang to Harbin radio-wave propagation path**

326 This transmitter operating at 6,600 kHz is located in the Republic of Korea at a great-circle range of ~910 km from the
327 receiver; it was switched off from 00:00 UT to 05:00 UT and from 22:20 UT to 24:00 UT.

328 On 29 September 2018, the Doppler shift showed fluctuations within the $\pm(0.2-0.3)$ Hz limits (Figure 10). Over the
329 next day, the Doppler spectrum broadening was observed to occur from 12:00 UT to 16:00 UT whereas the Doppler shift
330 exhibited quasi-sinusoidal ~20–24 min period, T , 0.1–0.2 Hz amplitude, f_{Da} , variations.

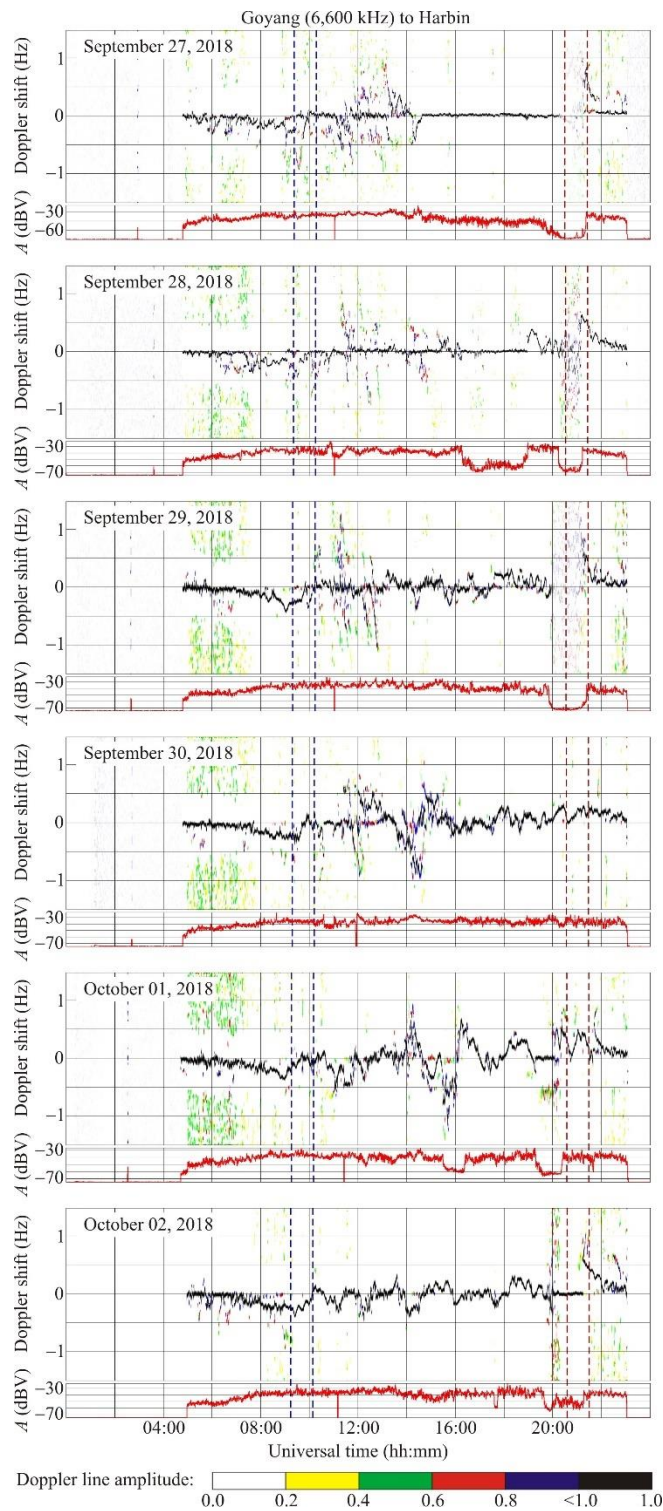
331 The Doppler ± 0.6 Hz spectrum broadening was observed to occur on 1 October 2018, while the Doppler spectra
332 exhibited ~20–120 min period, T , ~0.1–0.7 Hz amplitude, f_{Da} , variations; considerable, up to 20 dBV, variations were noted
333 in the signal amplitude.

334 On 2 October 2018, the Doppler shift exhibited significant, $\pm(0.2-0.3)$ Hz, variations, with a quasi-period, T , of 24
335 min and amplitude, f_{Da} , of ~0.2 Hz. Considerable fluctuations in the Doppler spectra, the Doppler shift, and in the signal
336 amplitude were noted on 3 October 2018. On 4 October 2018, from 14:00 UT to 20:00 UT, the Doppler shift showed
337 changes within the -0.3 Hz to 0.3 Hz limits, the quasi-sinusoidal processes were expressed weakly, and the signal amplitude
338 fluctuated wildly, by 30 dBV. On 5 October 2018, the variations in the Doppler shift did not exceed ± 0.2 Hz, the fluctuations
339 in the signal amplitude were also insignificant. The Doppler shift was observed to increase up to $\pm(0.3-0.5)$ Hz during the 6
340 October 2018 11:00–14:00 UT period, whereas from 15:00 UT to 18:00 UT, the quasi-sinusoidal oscillations in the Doppler
341 shift were observed to occur with a ~20 min period, T , and ~0.1 Hz amplitude, f_{Da} , while quasi-sinusoidal variations in the
342 signal amplitude, $A(t)$, were observed to occur with a ~55–80 min period, T , and ~7–8 dBV amplitude.

343 **6.6 Shijiazhuang to Harbin radio-wave propagation path**

344 This radio station operating at 9,500 kHz is located in the PRC at a great-circle range, R , of ~1,310 km from the receiver.

345 Figure 11 shows that the value of Doppler shift, $f_D(t)$, was close to zero on each night. The Doppler shift was
346 observed to be negative, attaining a minimum of $-(0.20-0.25)$ Hz, two to three hours before sunset at the ground. During the
347 UT night of 29 September 2018, the signal amplitude was observed to fluctuate wildly within the 20 dBV limits and to be
348 accompanied by fluctuations in the Doppler shift. A second ray shifted by -0.5 Hz with respect to the main ray was observed
349 to appear during the 16:00–20:00 UT period. From 30 September 2018 through 6 October 2018 UT nights, the signal
350 frequency approached the maximum usable frequency and ionospheric signal was about to penetrate the ionosphere, which
351 resulted in a 10–20 dBV decrease in the signal amplitude, whereas the Doppler spectra became low informative. These
352 circumstances have significantly hampered the search for the ionospheric response to the super typhoon action. Nevertheless,
353 the Doppler shift exhibited considerable, attaining -1 Hz, variations on 1 October 2018. Significant variations in the Doppler
354 shift were noted at the beginning of the 2 October 2018, UT night and after UT midnights on 3, 4, 5, and 6 October 2018; in
355 particular, the ray shifted by -0.5 Hz was recorded.



356
357
358

Figure 10: The same as in Figure 6 but for the Goyang to Harbin radio-wave propagation path at 6,600 kHz for the 27 September – 2 October 2018 period.

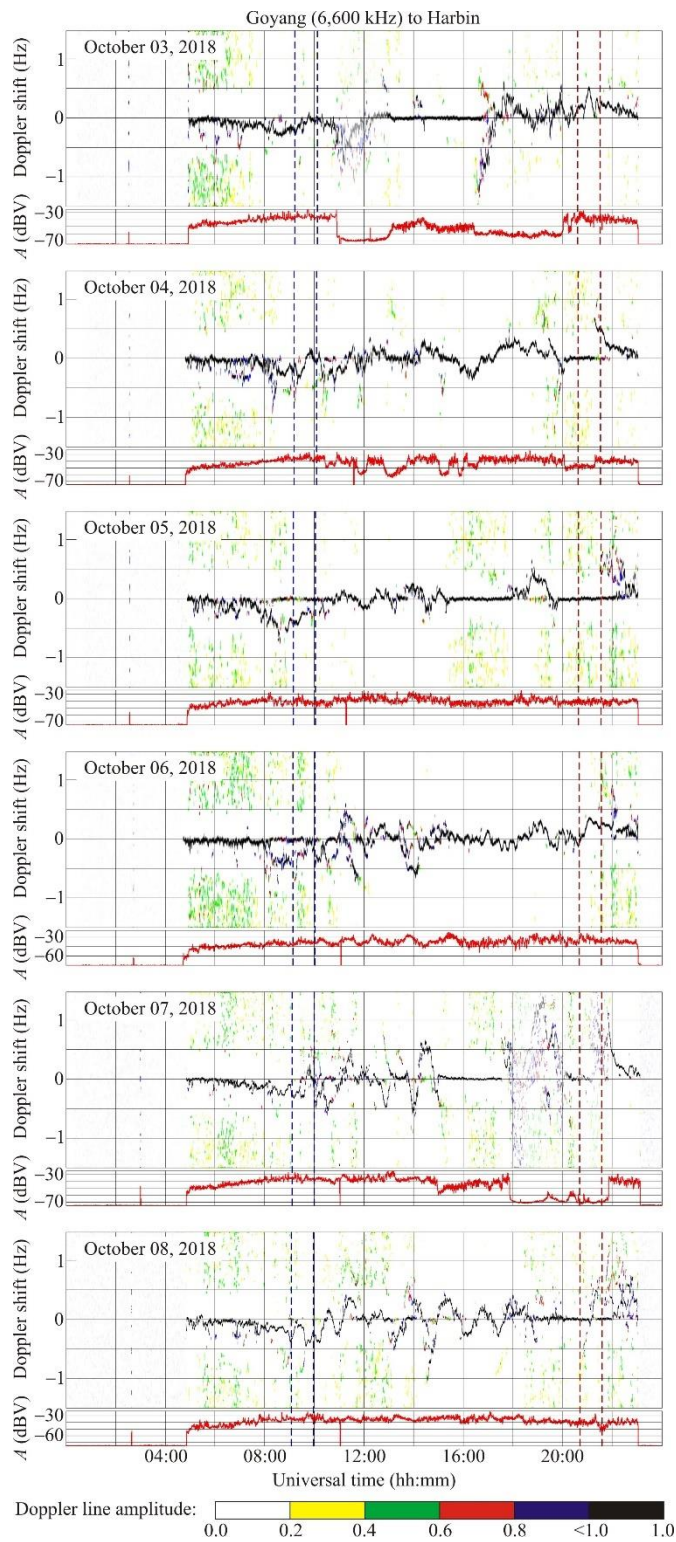
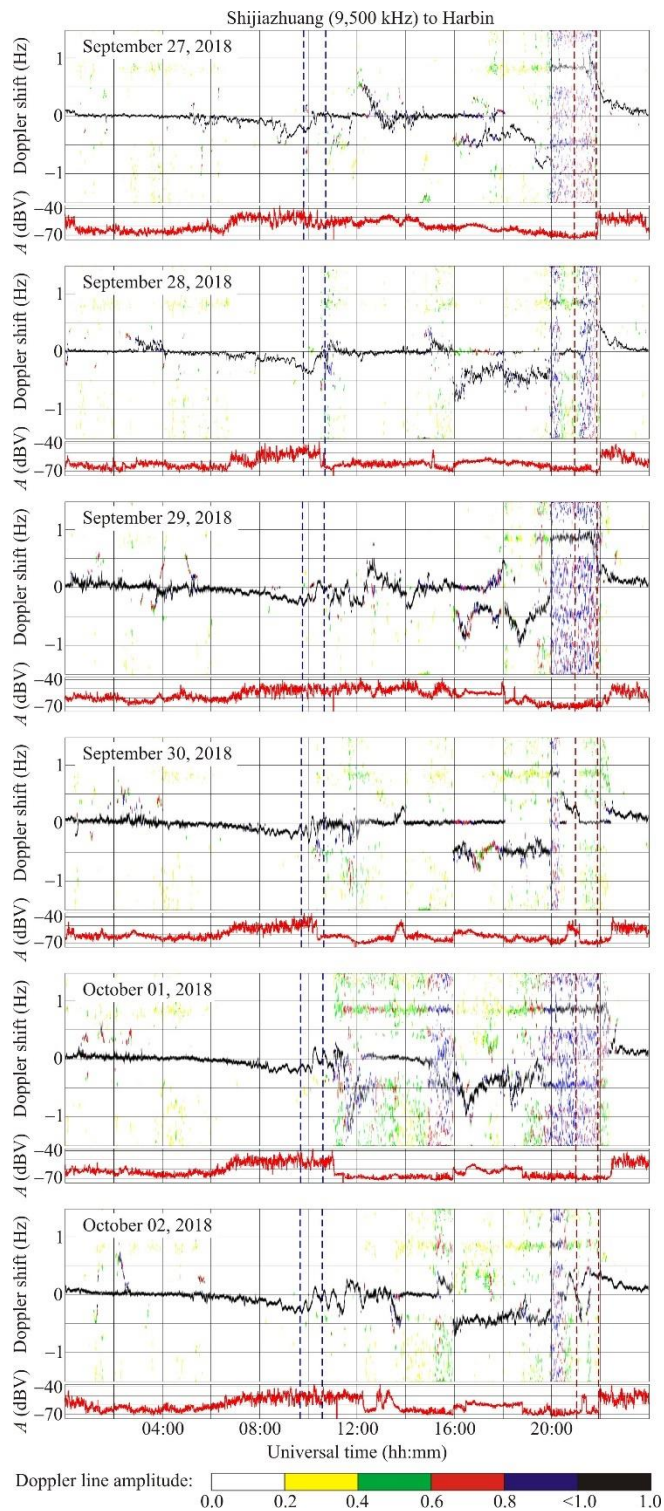


Figure 10: Continued for the 3–8 October 2018 period.



361
362
363

Figure 11: The same as in Figure 6 but for the Shijiazhuang to Harbin radio-wave propagation path at 9,500 kHz for the 27 September – 2 October 2018 period.

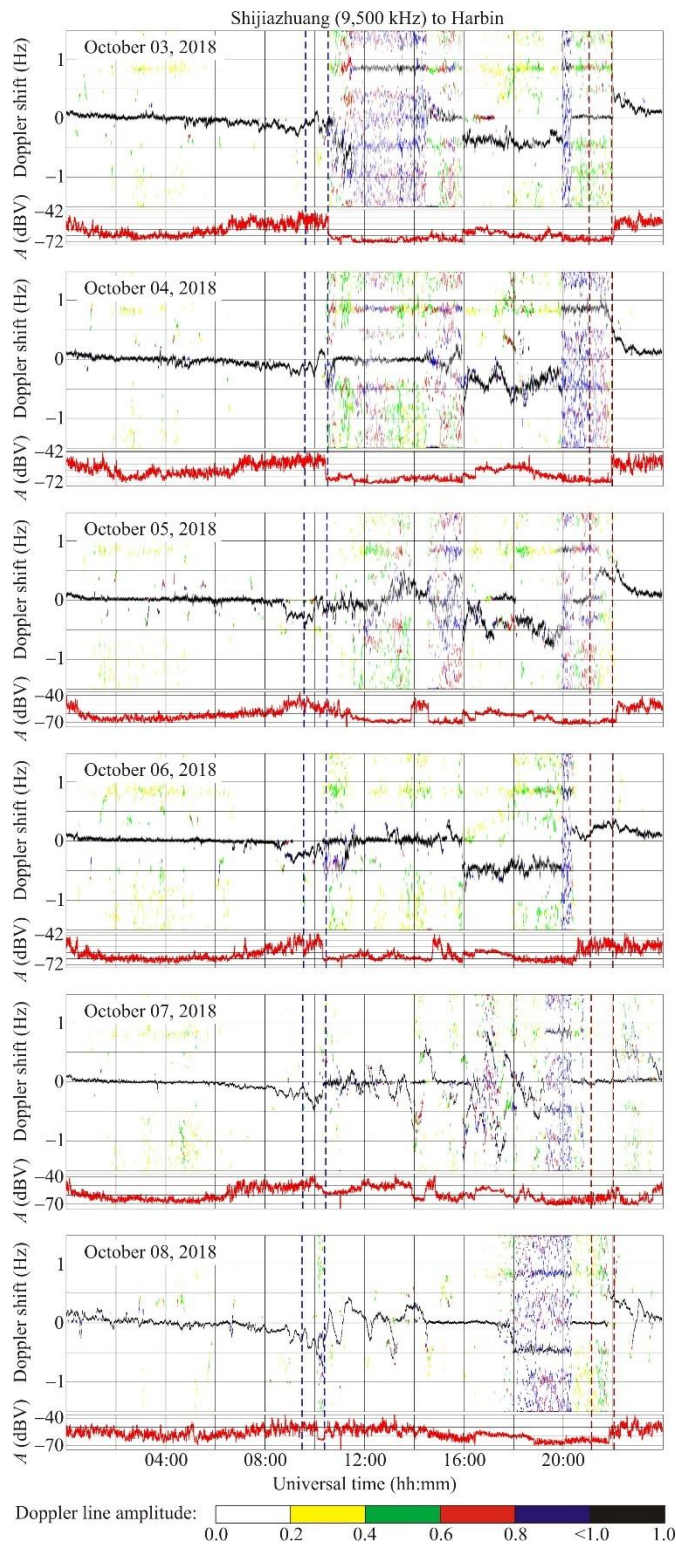


Figure 11: Continued for the 3–8 October 2018 period.

366 **6.7 Hohhot to Harbin radio-wave propagation path**

367 This transmitter operating at 9,520 kHz is located in the PRC at a great-circle range, R , of $\sim 1,340$ km; it was switched off
368 from 16:00 UT to $\sim 22:00$ UT.

369 The frequency of this radio wave became greater than the maximum usable frequency and the radio wave
370 penetrated the ionosphere during the second half of all nights (see Figure 12), the received signal was absent, and the
371 observation of the ionospheric dynamics became impossible. The Doppler spectra exhibited substantial variations (± 0.5 Hz)
372 on 29 September 2018, from 12:00 UT to 16:00 UT. On the UT night of 30 September 2018, the reflection of radio waves
373 took place from the sporadic E layer, resulting in $f_D(t) \approx 0$ Hz, and during the UT night of 1 October 2018, the Doppler shift
374 $f_D(t) \approx 0$ Hz as well. On the UT night of 2 October 2018, the Doppler shift showed changes from -0.3 Hz to 0.3 Hz, while the
375 signal amplitude exhibited considerable variability, up to 20 dBV. During the UT nights of 3–6 October 2018, the
376 measurements were ineffective, whereas $f_D(t) \approx 0$ Hz during sunlit hours.

377 **6.8 Yamata to Harbin radio-wave propagation path**

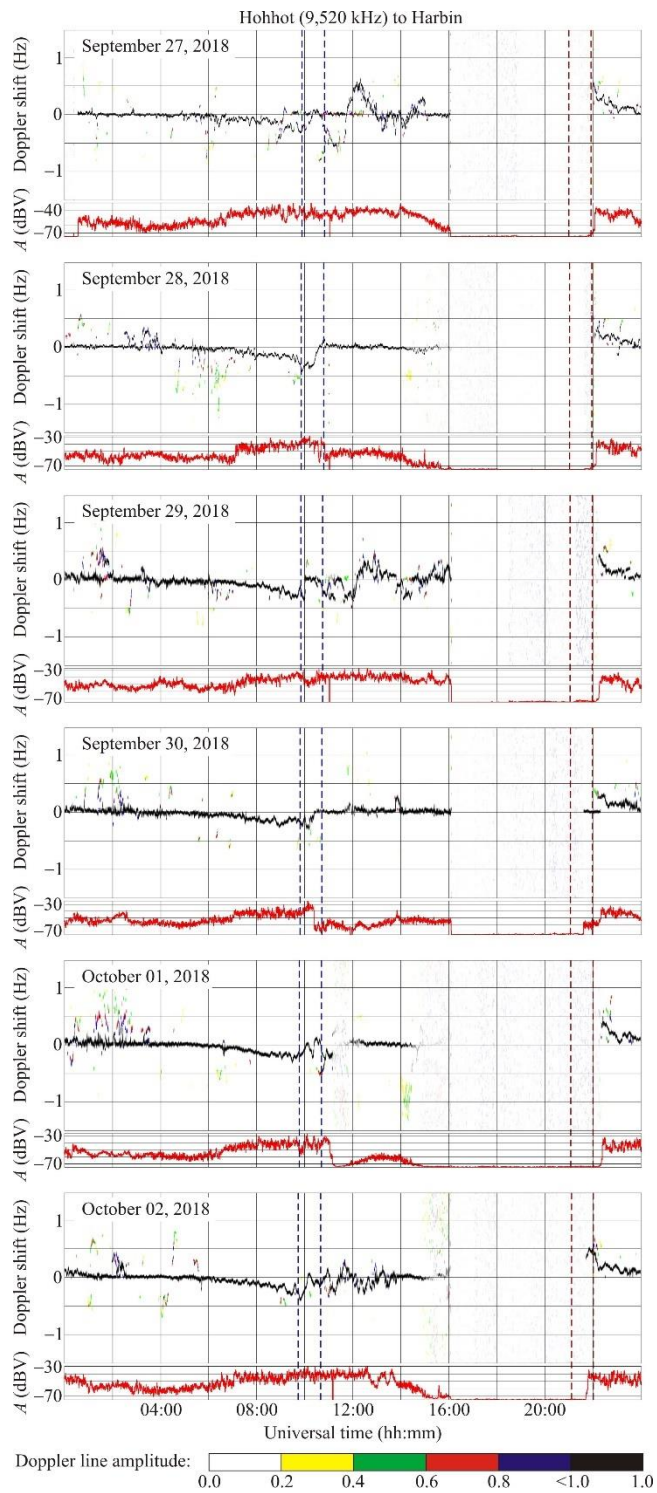
378 This radio station operating at 9,750 kHz is located in Japan at a great-circle range, R , of $\sim 1,570$ km. The transmitter was
379 switch off from 16:00 UT to $\sim 22:00$ UT.

380 A characteristic feature of these observations is that two signals were received, the Doppler shift of which were
381 shifted by 1 Hz from 29 September 2018 through 3 October 2018 and by 0.5 Hz from 4 October 2018 through 6 October
382 2018, as can be seen in Figure 13.

383 During all sunlit hours, the Doppler shift exhibited insignificant variations, whereas it became negative in the
384 evening. The Doppler shift and the Doppler spectrum variations were observed to be significant (from -1 Hz to 1 Hz) during
385 the UT nights of 29 and 30 September 2018. On 1 October 2018, the Doppler spectra exhibited diffuseness, while the signal
386 amplitude $A(t)$ variability was observed to attain 30 dBV. During the UT night of 2 October 2018, the Doppler shift was
387 observed to vary from -0.4 Hz to 0.4 Hz, while the variations in $A(t)$ also attained 30 dBV. The Doppler spectra and the
388 Doppler shift showed insignificant temporal variability on 3 and 4 October 2018; at the same time the signal amplitude
389 exhibited 20–30 dBV variations.

390 On 5 and 6 October 2018, the magnitude of the Doppler shift variations attained ± 0.2 Hz, while the signal
391 amplitude exhibited considerable changes in amplitude, up to 30 dBV.

392



393
394
395

Figure 12: The same as in Figure 6 but for the Hohhot to Harbin radio-wave propagation path at 9,520 kHz for the 27 September – 2 October 2018 period.

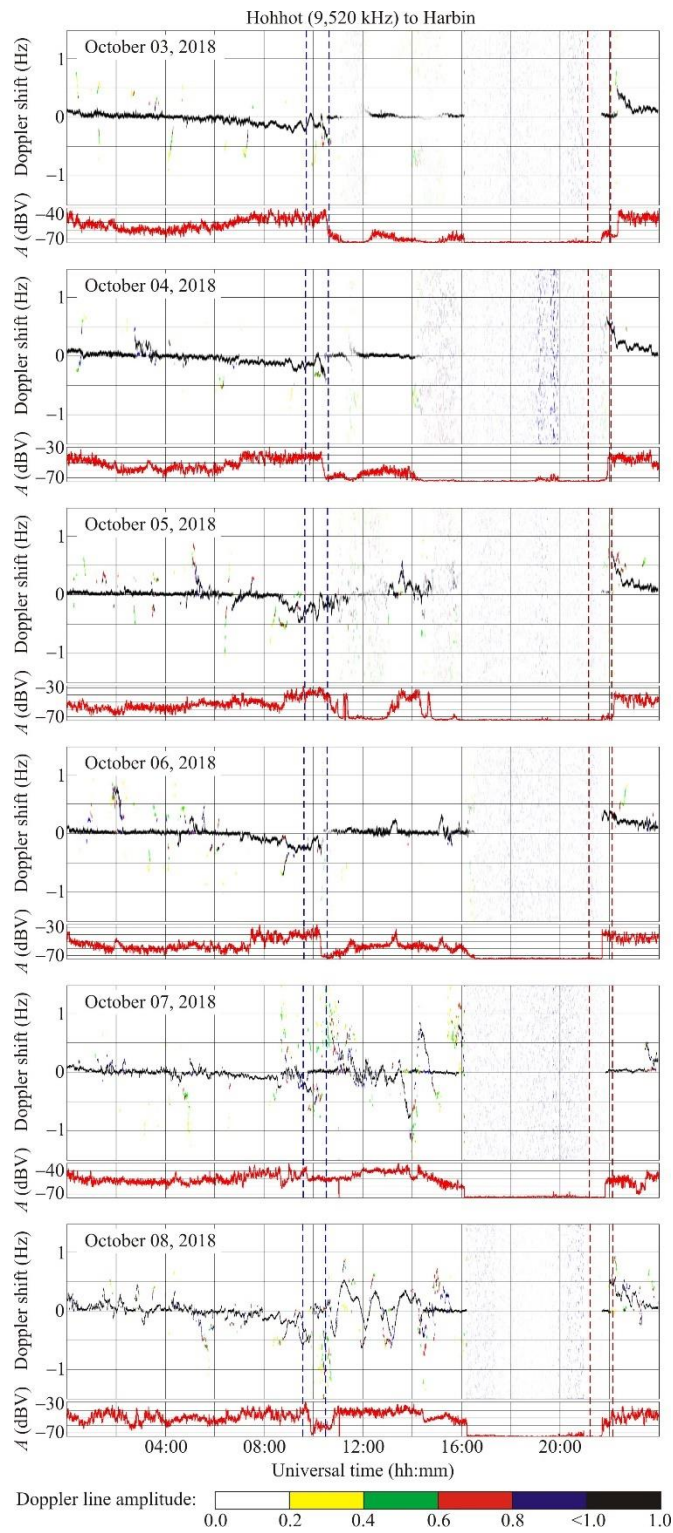
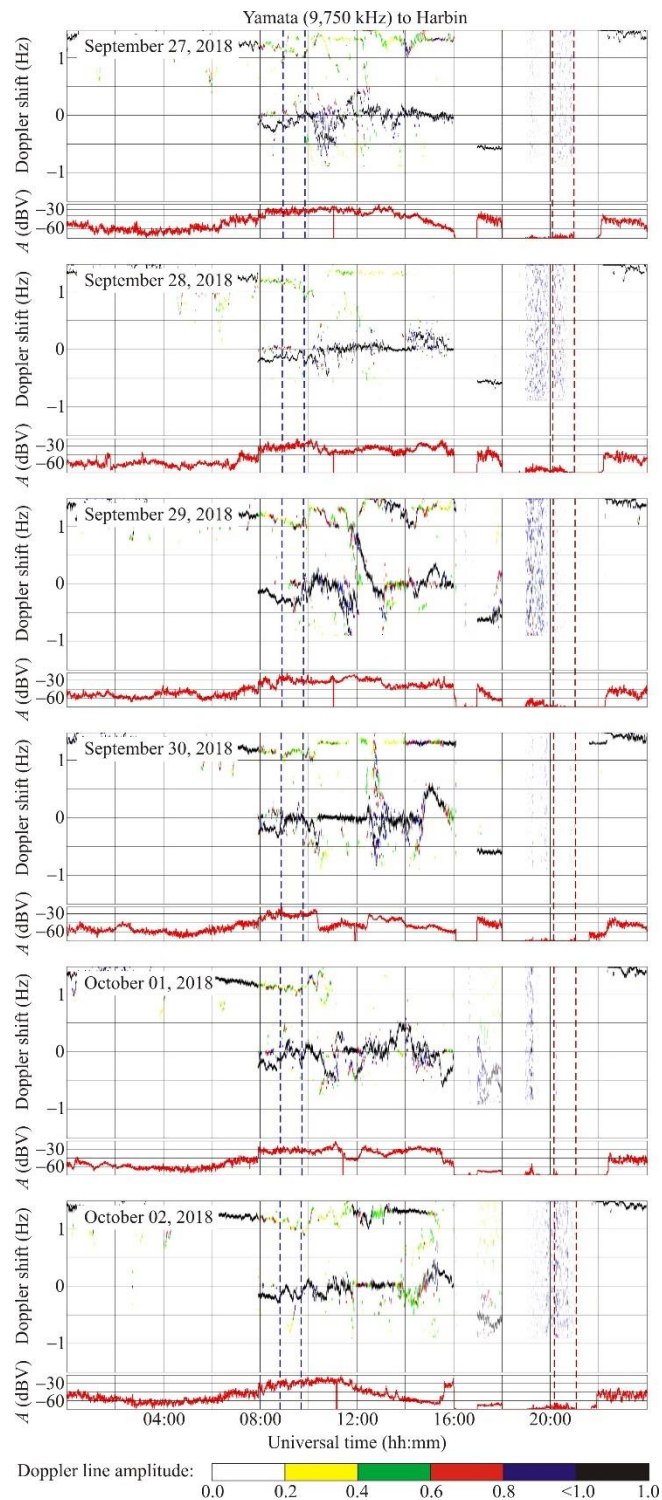


Figure 12: Continued for the 3–8 October 2018 period.



398

399 **Figure 13: The same as in Figure 6 but for the Yamata to Harbin radio-wave propagation path at 9,750 kHz for the 27 September**
 400 **– 2 October 2018 period.**

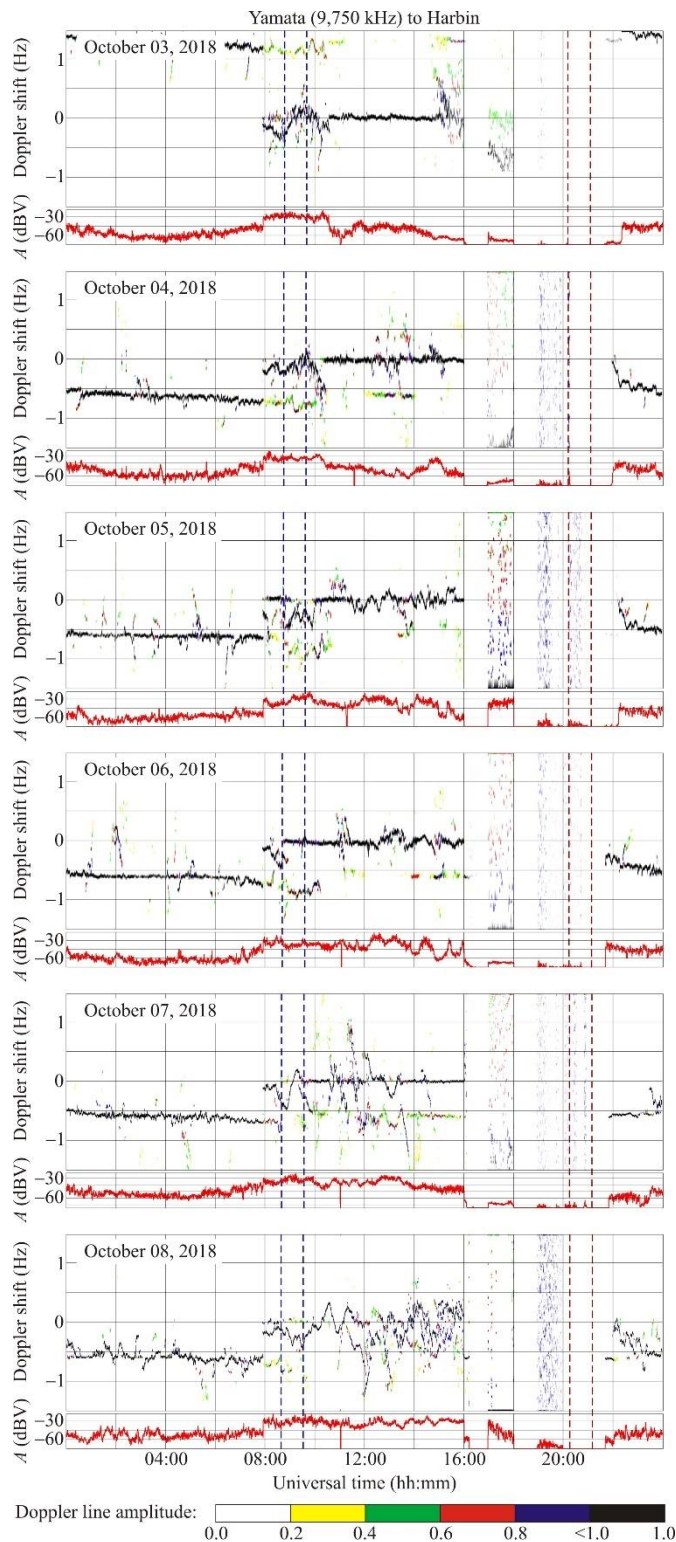


Figure 13: Continued for the 3–8 October 2018 period.

403 7 Discussion

404 7.1 Ionospheric effects from the super typhoon

405 The Doppler spectra and the Doppler shift observed during sunlit hours exhibited insignificant temporal variability through
406 the course of the typhoon action, since the radio waves in the ~6–10 MHz band were reflected from the ionospheric *E* region
407 or from the sporadic *E*. At night, the radio waves were reflected from the ionospheric *F* region, and the Doppler shift was
408 observed to reach maximum values of up to 0.5–1 Hz. The temporal variations in the Doppler shift were also generated by
409 the movement of the solar terminator.

410 The diurnal variations in the signal amplitude $A(t)$ were observed to attain 30 dBV, while $A(t)$ at night was three
411 orders of magnitude greater than $A(t)$ during the daytime, which is due to the disappearance of the absorbing *D* region.

412 In order to find out that the observed Doppler shift variations are associated with the typhoon, the Doppler
413 variations were low-pass filtered, and the Doppler variations, with periods of greater than 40 min, were found to occur
414 during the 2 October 2018 10:00–14:00 UT period, along all propagation paths. A characteristic feature, a fading, which
415 could be traced in all temporal dependences of the identified Doppler variations, was selected for analyzing. The UT
416 moments, t^* , when this feature arrived at each propagation path midpoint are presented in Table 4. At 12:00 UT on 2
417 October 2018, the typhoon center was located at (18.9° N, 131.2° E) at the distances D from the propagation path midpoints,
418 with the midpoint of the 9.750 MHz propagation path being closest (2,492 km) to the typhoon center, while other midpoints
419 were found to be at $(2,492 + \Delta D)$ km ranges, where the characteristic feature arrived with time delays of Δt with respect to
420 the arrival time at the 9.750 MHz midpoint. As can be seen in Table 4, the ΔD and Δt yield the values of the apparent speeds,
421 v , quite close to each other. These estimates testify to the adequacy of the assumption that the propagation of the
422 disturbances from the typhoon is the cause of the observed Doppler shift variations. The mean value of the speed of the
423 strongest, 60 – 70 min, period component, estimated to be $205 \pm 6 \text{ m s}^{-1}$, corresponds to a TID with wavelength equal to
424 approximately 800 km. Taking a look at the Kong-Rey trajectory in Figure 1a, one can notice that the TIDs traveled
425 northwestward in this case, contrary to the southwestward direction observed in this area of the world in the climatological
426 study by Shiokawa et al. (2003).

427

428

429 Table 4. Distances D over which TIDs traveled at apparent speeds v and arrived at the propagation pass midpoints
 430 from the center of typhoon Kong-Rey with relative time delays Δt at the UT moments t^* .

f (MHz)	6.015	6.055	6.080	6.175	6.600	9.500	9.520	9.750
D (km)	2,574	2,454	3,296	2,826	2,595	2,803	2,963	2,492
ΔD (km)	120	38	842	372	141	349	509	0
t^* (UT)	11:00	10:53	12:00	11:20	11:03	11:15	11:25	10:50
Δt (min)	10	3	70	30	12	28	38	–
v (m s ⁻¹)	200	210	200	205	195	205	220	–

431

432 The ionospheric effects from super typhoon Kong-Rey are discussed further below. Super typhoon Kong-Rey's
 433 power gained a maximum value during the second half of 1 October 2018 and, consequently, the Doppler shift and the
 434 Doppler spectra showed the greatest variations during the UT night of 1 October 2018, despite the propagation path
 435 midpoints were located ~2,800–3,300 km away from the super typhoon. As should be expected, the greatest effects were
 436 observed to occur at the propagation path midpoints located closest to the typhoon, i.e., in the signals transmitted from the
 437 radio stations at Chiba/Nagara, Goyang, Yamata (Japan) and Hwaseong (Republic of Korea). At the same time, the
 438 ionospheric effects from super typhoon Kong-Rey were absent along the Hohhot to Harbin radio-wave propagation path
 439 located at the farthest range to the typhoon on 1 October 2018.

440 On 2 October 2018, super typhoon Kong-Rey moved closer to the propagation path midpoints by only ~600 km;
 441 however, its power reduced by a factor of approximately 2 during the night. As a result, the ionospheric response to the
 442 typhoon action reduced noticeably, and the ionospheric effects were either weak or absent during the daytime of 2 October
 443 2018, as well as during sunlit hours on 3 and 4 October 2018.

444 Figure 1a shows that a surge in the typhoon's power (marked in red) appeared during the time interval between the
 445 noon of 5 and 6 October 2018, when the typhoon and the propagation path midpoints were at ~1,000–1,500 km distances
 446 apart. Consequently, increases in the amplitude of Doppler shift and, partly, in the signal amplitude variations were observed
 447 to occur on 5 October 2018 as well as along a number of propagation paths on 6 October 2018 despite the typhoon's power
 448 was reduced by a factor of ~3, as compared to that observed on 1 October 2018.

449 7.2 Wavelike disturbances

450 Wavelike disturbances in the ionosphere can be seen even on 29 and 30 September 2018, whereas on 1–2 and 5–6 October
 451 2018, a noticeably increase (by a factor of ~2–3) in the amplitude of Doppler shift and in the signal amplitude variations, in a
 452 number of cases, were observed to occur. Based on the periods (from 20 min to 120 min), the wavelike disturbances in the
 453 ionosphere are caused by atmospheric gravity waves (Gossard and Hooke, 1975).

454 The basic parameters of wave disturbances associated with the action of typhoon Kong-Rey are presented in Table 5.

455

456 Table 5.

457 Basic parameters of wave disturbances in October 2018.

Radio-wave propagation path	Date			
	1 October	2 October	5 October	6 October
Hwaseong to Harbin	$T = 120$; 24 min $f_{Da} = 0.4$; 0.1 Hz	$T = 120$; 24 min $f_{Da} = 0.25$; 0.1 Hz	$T = 100$ –110; 15 min $f_{Da} = 0.1$ –0.2; 0.05 Hz	$T = 120$; 20 min $f_{Da} = 0.3$; 0.05 Hz
Chiba/Nagara to Harbin	$T = 60$ –80 min $f_{Da} = 0.4$ Hz	$T = 20$ –30 min $f_{Da} = 0.2$ –0.3 Hz	$T = 30$ –40 min $f_{Da} = 0.3$ Hz	$T = 100$ min $f_{Da} = 0.3$ Hz
Hailar/Nanmen to Harbin	$T = 80$; 15 min $f_{Da} = 0.4$; 0.05 Hz	$T = 40$ –50 min $f_{Da} = 0.2$ –0.3 Hz	$T = 40$; 20 min $f_{Da} = 0.2$ –0.3 Hz	$T = 40$ –60 min $f_{Da} = 0.1$ –0.2 Hz
Beijing to Harbin	$T = 30$ –40; 20–24 min $f_{Da} = 0.2$; 0.1 Hz	$T = 60$; 20–25 min $f_{Da} = 0.2$; 0.1 Hz	$T = 40$ –60; 20 min $f_{Da} = 0.2$; 0.05 Hz	$T = 80$; 20–30 min $f_{Da} = 0.2$ Hz
Goyang to Harbin	$T = 120$; 30–40 min $f_{Da} = 0.3$; 0.1 Hz	$T = 40$ –60; 30 min $f_{Da} = 0.2$; 0.1 Hz	$T = 80$ –90 min $f_{Da} = 0.2$ Hz	$T = 100$ –120; 20 min $f_{Da} = 0.4$; 0.1 Hz
Shijiazhuang to Harbin	$T = 120$ min $f_{Da} = 0.3$ Hz	$T = 60$ min $f_{Da} = 0.3$ Hz	$T = 120$ min $f_{Da} = 0.3$ Hz	$T = 120$ min $f_{Da} = 0.1$ Hz
Hohhot to Harbin	–	$T = 120$; 40–50 min $f_{Da} = 0.2$ –0.3 Hz	–	–
Yamata to Harbin	$T = 65$ –80 min $f_{Da} = 0.3$ –0.4 Hz	$T = 80$ min $f_{Da} = 0.2$ Hz	$T = 40$; 25–30 min $f_{Da} = 0.2$; 0.1 Hz	$T = 70$ min $f_{Da} = 0.2$ Hz

458

459 Given known f_{Da} and T , the amplitude, δ_{Na} , of quasi-sinusoidal variations in the electron density can be estimated on
460 a relative scale. To do this, one can use the following equation (Chernogor et al., 2020; Guo et al., 2020):

$$461 \quad \delta_{Na} = \frac{K}{4\pi} \frac{cT}{L} \frac{f_{Da}}{f} \quad (1)$$

462 where

$$463 \quad K = \frac{1 + \cos \theta}{2(1 + 2\xi \tan^2 \theta) \cos^2 \theta}; \quad \xi = \frac{z_r - z_0}{r_0}; \quad \tan \theta = \frac{R}{2z_r}, \quad (2)$$

464 c is the speed of light, θ is the angle of incidence with respect to the vertical at the basis of the ionosphere, z_0 is the altitude
 465 of the beginning of the layer giving a contribution to the Doppler shift, z_r is the altitude of reflection, r_0 is the mean Earth's
 466 radius, L is the thickness of the atmospheric region giving a contribution to the Doppler shift.

467 Substituting $T \approx 20$ min and $f_{Da} \approx 0.1$ Hz in (1) and taking into account (2) yield $\delta_{Na} \approx 0.4\%$. If $T \approx 30$ min and
 468 $f_{Da} \approx 0.2$ Hz, then $\delta_{Na} \approx 1.2\%$. Also, $T \approx 60$ min and $f_{Da} \approx 0.5$ Hz give $\delta_{Na} \approx 6\%$. Thus, the super typhoon action in the
 469 ionosphere leads to an increase in the amplitude of variations in the electron density, depending on the period of quasi-
 470 sinusoidal disturbances, by a fraction to several per cent.

471 In addition, the amplitude of quasi-sinusoidal variations in the Doppler shift is observed to increase along many
 472 propagation paths under the joint action of the super typhoon and dusk terminator passing by. Consequently, the synergistic
 473 action of the dusk terminator and typhoons takes place in the ionosphere. An effect analogous to the one mentioned above
 474 was observed earlier by Edemsky and Yasyukevich (2018) who made use of GPS technology for probing wave disturbances.
 475 During the dawn terminator, such an effect is not reliably observed.

476 **7.3 Comparison of ionospheric effects from typhoons**

477 A multifrequency multiple path coherent software defined radio system developed at the Harbin Engineering University has
 478 been in routine use for several years for determining variations in ionospheric parameters and in radio wave characteristics in
 479 the 5–10 MHz band, which accompanied the movement of super typhoon Hagibis (Chernogor et al., 2021), Ling-Ling and
 480 Faxai (Chernogor et al., 2022), Lekima (Zheng et al., 2022), Kong-Rey, etc. The response of the ionosphere to typhoon
 481 action has been shown to be dependent not only on the parameters of typhoons, but also on the state of atmospheric and
 482 space weather, local time, and on other geophysical parameters. Not only are common manifestations in the response found,
 483 but also individual manifestations that are characteristic of a particular super typhoon. The common manifestations include:
 484 (1) the aperiodic (chaotic) character of the ionospheric response; (2) the magnitude of the response shows an apparent
 485 abatement with increasing distance between the typhoon and the propagation path midpoints; (3) the response exhibits a
 486 maximum with distance (between the typhoon and the propagation path midpoint) approaching a minimum; (4) Doppler shift
 487 spectrum broadening up to ± 1 Hz due to an increase in the number of rays; (5) the occurrence of quasi-sinusoidal variations
 488 in the Doppler shift with amplitudes of ~ 0.1 – 0.5 Hz and periods of 2–5 min and 10–100 min; (6) the generation or
 489 enhancement of infrasound (periods, T , of ~ 2 – 5 min) and atmospheric gravity waves (periods, T , of ~ 10 – 100 min); (7)

490 disturbances of the electron density amplitudes in these wave fields attaining ~1 % and ~10%, respectively, and greater; (8)
491 aperiodic perturbations (for the most part, increases) in the electron density that could attain a few tens of per cent.

492 The instrument created by the authors of this paper permitted the confirmation of only one mechanism of affecting
493 the ionosphere with a typhoon, i.e., the acoustic–atmospheric gravity waves. To reveal electromagnetic and electric
494 mechanisms, one should employ other instruments.

495 **8 Conclusions**

496 (1) The Harbin Engineering University multifrequency multiple path coherent software defined radio system for probing the
497 ionosphere at oblique incidence have been used to detect the ionospheric effects over the People’s Republic of China during
498 the 27 September 2018 to 8 October 2018 period encompassing the super typhoon Kong-Rey event. The movement of the
499 super typhoon was accompanied by significant variations in radio wave characteristics in the 5–10 MHz band.

500 (2) The ionospheric response to the super typhoon action was clearly observed to occur on 1–2 October 2018 when
501 the typhoon was 2,800–3,300 km away from the propagation path midpoints and super typhoon Kong-Rey’s energy gained a
502 maximum value, and on 5–6 October 2018 when the typhoon was 1,000–1,500 km away from the midpoints and its energy
503 decreased by a factor of approximately 3.

504 (3) The ionospheric effects are more pronounced along the nearest propagation paths, whereas no effect is detected
505 along the propagation path at the greatest distance from the typhoon.

506 (4) The super typhoon action on the ionosphere was accompanied by the generation or amplification of quasi-
507 sinusoidal variations in the Doppler shift by a factor of 2–3, as well as by noticeable variations in the signal amplitude. The
508 Doppler spectra were observed to broaden in a number of cases.

509 (5) The period of wave perturbations exhibited variability in the ~20 min to ~120 min range. This meant that the
510 perturbations in the ionospheric electron density were caused by atmospheric gravity waves (AGWs) generated by the
511 typhoon: the greater the AGW period, the greater the Doppler shift. As the period increased from 20 min to 120 min, the
512 Doppler shift amplitudes increased from ~0.1 Hz to 0.5–1 Hz.

513 (6) As the AGW period increases from 20 min to 60 min, the amplitude of quasi-sinusoidal variations in the
514 electron density increases from 0.4 to 6 per cent.

515 (7) The most important mechanism of affecting the ionosphere has been confirmed to be associated with the
516 generation of the 20–120 min period AGW by the typhoon.

517 (8) The Doppler measurements have shown that dusk terminators and the super typhoon acted synergistically to
518 amplify the ionospheric response to these sources of energy.

519

520 **Code Availability.** Software for Passive 14-Channel Doppler Radar may be obtained from the website at
521 <https://dataverse.harvard.edu/dataset.xhtml?persistentId=doi:10.7910/DVN/MTGAVH> (Garmash, 2021).

522

523 **Data Availability.** The data sets discussed in this paper may be obtained from the website at
524 <https://dataverse.harvard.edu/dataset.xhtml?persistentId=doi:10.7910/DVN/VHY0L2> (Garmash, 2022).

525

526

527 **Author Contribution**

528 **Conceptualization:** Leonid Chernogor; **Data Curation:** Qiang Guo and Kostiantyn Garmash; **Formal Analysis:** All
529 Authors: Yu Zheng, Leonid Chernogor, Kostiantyn Garmash, Qiang Guo, Victor Rozumenko; **Funding Acquisition:** Qiang
530 Guo; **Investigation:** Qiang Guo and Kostiantyn Garmash; **Methodology:** Leonid Chernogor; **Project Administration:**
531 Qiang Guo; **Resources:** Qiang Guo; **Software:** Kostiantyn Garmash; **Supervision:** Leonid Chernogor; **Validation:** All
532 Authors: Leonid Chernogor, Kostiantyn Garmash, Qiang Guo, Victor Rozumenko, Yu Zheng; **Visualization:** Kostiantyn
533 Garmash, Yu Zheng; **Writing – original draft:** All Authors: Leonid Chernogor, Kostiantyn Garmash, Qiang Guo, Victor
534 Rozumenko, Yu Zheng; **Writing review & editing:** All Authors: Leonid Chernogor, Kostiantyn Garmash, Qiang Guo,
535 Victor Rozumenko, Yu Zheng.

536

537 **Competing Interests.** The authors declare that they have no conflict of interests

538

539 **Acknowledgments**

540 This article makes use of data on typhoon 201825 Kong-Rey recorded by the Japan Meteorological Agency and published at
541 <http://agora.ex.nii.ac.jp/digital-typhoon/summary/wnp/s/201825.html.en>. The solar wind parameters were retrieved from the
542 Goddard Space Flight Center Space Physics Data Facility <https://omniweb.gsfc.nasa.gov/form/dx1.html>. This research also
543 draws upon data provided by the WK546 URSI code ionosonde in the city of Wakkanai (45.16° N, 141.75° E), Japan, URL:
544 https://wdc.nict.go.jp/IONO/HP2009/contents/Ionosonde_Map_E.html (ionosonde data are retrieved from
545 <http://wdc.nict.go.jp/IONO/HP2009/ISDJ/index-E.html>). Work by Qiang Guo and Yu Zheng was supported by the National
546 Key R&D Plan Strategic International Science and Technology Cooperation and Innovation (2018YFE0206500). Work by
547 L. F. Chernogor was supported by the National Research Foundation of Ukraine for financial support (project 2020.02/0015,
548 “Theoretical and experimental studies of global disturbances from natural and technogenic sources in the Earth-atmosphere-
549 ionosphere system”). Work by L. F. Chernogor and V. T. Rozumenko was supported by the Ukraine state research project
550 #0121U109881, and work by K. P. Garmash was supported by the Ukraine state research project #0121U109882.

551 **References**

- 552 Afraimovich, E. L., Voeykov, S. V., Ishin, A.B., Perevalova, N. P., and Ruzhin, Yu. Ya.: Variations in the total electron
553 content during the powerful typhoon of August 5–11, 2006, near the southeastern coast of China, *Geomag. Aeron.*, 48, 674–
554 679, <https://doi.org/10.1134/S0016793208050113>, 2008.
- 555 Bortnik, J., Inan, U. S., and Bell, T. F.: Temporal signatures of radiation belt electron precipitation induced by lightning-
556 generated MR whistler waves: 1. Methodology, *J. Geophys. Res.*, 111, A02204, <https://doi.org/10.1029/2005JA011182>,
557 2006.
- 558 Boška, J. and Šauli, P.: Observations of gravity waves of meteorological origin in the *F*-region ionosphere,
559 *Phys. Chem. Earth, Part C*, 26, 425–428, [https://doi.org/10.1016/S1464-1917\(01\)00024-1](https://doi.org/10.1016/S1464-1917(01)00024-1), 2001.
- 560 Chen, J., Zhang, X., Ren, X., Zhang, J., Freeshah, M., and Zhao, Z.: Ionospheric disturbances detected during a typhoon
561 based on GNSS phase observations: a case study for typhoon Mangkhut over Hong Kong, *Adv. Space Res.*, 66, 1743–1753,
562 <https://doi.org/10.1016/j.asr.2020.06.006>, 2020.
- 563 Chernigovskaya, M. A., Shpynev, B. G., and Ratovsky, K. G.: Meteorological effects of ionospheric disturbances from
564 vertical radio sounding data, *J. Atmos. Solar-Terr. Phys.*, 136, 235–243, <https://doi.org/10.1016/j.jastp.2015.07.006>, 2015.
- 565 Chernogor, L. F.: The tropical cyclone as an element of the Earth – atmosphere – ionosphere – magnetosphere system
566 (in Russian), *Space Sci. Tech.*, 12, 16–26, <https://doi.org/10.15407/knit2006.02.016>, 2006.
- 567 Chernogor, L. F.: Advanced Methods of Spectral Analysis of Quasiperiodic Wave-Like Processes in the Ionosphere:
568 Specific Features and Experimental Results, *Geomag. Aeron.*, 48, 652 – 673,
569 <https://doi.org/10.1134/S0016793208050101>, 2008.
- 570 Chernogor, L. F.: *Physics and Ecology of Disasters* (in Russian), V. N. Karazin Kharkiv National University Publ., Kharkiv,
571 Ukraine, 2012.
- 572 Chernogor, L. F., Garmash, K. P., Guo, Q., Luo, Y., Rozumenko, V. T., and Zheng, Y.: Ionospheric storm effects over the
573 People’s Republic of China on 14 May 2019: Results from multipath multi-frequency oblique radio sounding,
574 *Adv. Space Res.*, 66, 226 – 242, <https://doi.org/10.1016/j.asr.2020.03.037>, 2020.
- 575 Chernogor L.F., Garmash K.P., Guo Q., Rozumenko V.T., Zheng Y., and Luo Y.: Supertyphoon Hagibis action in the
576 ionosphere on 6–13 October 2019: Results from multi-frequency multiple path sounding at oblique incidence, *Adv. Space*
577 *Res.*, 67, 2439–2469, <https://doi.org/10.1016/j.asr.2021.01.038>, 2021.
- 578 Chernogor, L. F., Garmash, K. P., Guo, Q., Rozumenko, V. T., Zheng, Y., and Luo, Y.: Disturbances in the ionosphere that
579 accompanied typhoon activity in the vicinity of China in September 2019, *Radio Sci.*, 57. e2022RS007431,
580 <https://doi.org/10.1029/2022RS007431>, 2022.
- 581 Chou, M. Y., Lin, C. C. H., Yue, J., Tsai, H. F., Sun, Y. Y., Liu, J. Y., and Chen, C. H.: Concentric traveling ionosphere
582 disturbances triggered by Super Typhoon Meranti (2016), *Geophys. Res. Lett.*, 44, 1219–1226,
583 <https://doi.org/10.1002/2016GL072205>, 2017.

584 Chum, J., Liu, J.-Y., Šindelářová, K., and Podolská, T.: Infrasound in the ionosphere from earthquakes and typhoons,
585 *J. Atmos. Sol.–Terr. Phys.*, 171, 72–82, <https://doi.org/10.1016/j.jastp.2017.07.022>, 2018.

586 Das, B., Sarkar, S., Haldar, P. K., Midya, S. K., and Pal, S.: *D*-region ionospheric disturbances associated with the Extremely
587 Severe Cyclone Fani over North Indian Ocean as observed from two tropical VLF stations, *Adv. Space Res.*, 67, 75–86,
588 <https://doi.org/10.1016/j.asr.2020.09.018>, 2021.

589 Drobyazko, I. N., and Krasil'nikov, V. N.: Generation of acoustic-gravity waves by atmospheric turbulence. *Radiophysics*
590 *and Quantum Electronics*, 28, 946–952. <https://doi.org/10.1007/bf01040717>, 1985.

591 Edemsky, I. K. and Yasyukevich, A. S.: Observing wave packets generated by solar terminator in TEC during typhoons,
592 *Solar-Terr. Phys.*, 4, 33–40, <https://doi.org/10.12737/szf-42201806>, 2018.

593 Fišer, J., Chum, J., and Liu, J.-Y.: Medium-scale traveling ionospheric disturbances over Taiwan observed with HF Doppler
594 sounding, *Earth, Planet. Space.*, 69, 131, <https://doi.org/10.1186/s40623-017-0719-y>, 2017.

595 Freeshah, M., Zhang, X., Şentürk, E., Adil, M. A., Mousa, B. G., Tariq, A., Ren, X., and Refaat, M.: Analysis of
596 Atmospheric and Ionospheric Variations Due to Impacts of Super Typhoon Mangkhut (1822) in the Northwest Pacific
597 Ocean, *Remote Sens.*, 13, 661, <https://doi.org/10.3390/rs13040661>, 2021.

598 Frissell, N. A., Baker, J. B. H., Ruohoniemi, J. M., Gerrard, A. J., Miller, E. S., Marini, J. P., West, M. L., and Bristow, W.
599 A.: Climatology of medium-scale traveling ionospheric disturbances observed by the midlatitude Blackstone SuperDARN
600 radar, *J. Geophys. Res. Space Physics*, 119, 7679–7697, doi:[10.1002/2014JA019870](https://doi.org/10.1002/2014JA019870), 2014.

601 Fukushima, D., Shiokawa, K., Otsuka, Y., and Ogawa, T.: Observation of equatorial nighttime medium-scale traveling
602 ionospheric disturbances in 630-nm airglow images over 7 years, *J. Geophys. Res.*, 117, A10324,
603 doi:[10.1029/2012JA017758](https://doi.org/10.1029/2012JA017758), 2012.

604 Garmash, K.: Software for Passive 14-Channel Doppler Radar, <https://doi.org/10.7910/DVN/MTGAVH>, Harvard Dataverse,
605 V1, <https://dataverse.harvard.edu/dataset.xhtml?persistentId=doi:10.7910/DVN/MTGAVH>, 2021.

606 Garmash, K.: RAW Data on Parameters of Ionospheric HF Radio Waves Propagated Over China During the September 29 –
607 6 October 2018 Typhoon Activity in the Vicinity of China, <https://doi.org/10.7910/DVN/VHY0L2>, Harvard Dataverse, V1
608 <https://dataverse.harvard.edu/dataset.xhtml?persistentId=doi:10.7910/DVN/VHY0L2>, 2022.

609 Gavrilov, N. M. and Kshevetskii, S. P.: Dynamical and thermal effects of nonsteady nonlinear acoustic-gravity waves
610 propagating from tropospheric sources to the upper atmosphere, *Adv. Space Res. (Includes COSPAR Information Bulletin)*,
611 56, 1833–1843, <https://doi.org/10.1016/j.asr.2015.01.033>, 2015.

612 Gossard, E. E. and Hooke, W. H.: *Waves in the Atmosphere: Atmospheric Infrasound and Gravity Waves, Their Generation*
613 *and Propagation*, Elsevier Scientific Publ. Co., Amsterdam, Netherlands, 1975.

614 Guo, Q., Zheng, Y., Chernogor, L. F., Garmash, K. P., and Rozumenko, V. T.: Ionospheric processes observed with the
615 passive oblique-incidence HF Doppler radar, *Visnyk of V.N. Karazin Kharkiv National University, series “Radio Physics*
616 *and Electronics”*, 30, 3–15, <https://doi.org/10.26565/2311-0872-2019-30-01>, 2019a.

617 Guo, Q., Chernogor, L. F., Garmash, K. P., Rozumenko, V. T., and Zheng, Y.: Dynamical processes in the ionosphere
618 following the moderate earthquake in Japan on 7 July 2018, *J. Atmos. Solar-Terr. Phys.*, 186, 88–103,
619 <https://doi.org/10.1016/j.jastp.2019.02.003>, 2019b.

620 Guo, Q., Chernogor, L. F., Garmash, K. P., Rozumenko, V. T., and Zheng, Y.: Radio Monitoring of Dynamic Processes in
621 the Ionosphere Over China During the Partial Solar Eclipse of 11 August 2018, *Radio Sci.*, 55, e2019RS006866,
622 <https://doi.org/10.1029/2019RS006866>, 2020.

623 Hickey, M. P., Schubert, G., and Walterscheid, R. L.: Acoustic wave heating of the thermosphere, *J. Geophys. Res.*, 106,
624 21543–21548, <https://doi.org/10.1029/2001JA000036>, 2001.

625 Hickey, M. P., Walterscheid, R. L., and Schubert, G.: Gravity wave heating and cooling of the thermosphere: Roles of the
626 sensible heat flux and viscous flux of kinetic energy, *J. Geophys. Res.*, 116, A12326,
627 <https://doi.org/10.1029/2011JA016792>, 2011.

628 Hung, R. J. and Kuo, J. P.: Ionospheric observation of gravity-waves associated with Hurricane Eloise, *J. Geophys.*, 45, 67–
629 80, <https://journal.geophysicsjournal.com/JofG/article/view/173>, 1978.

630 Hocke, K. and Schlegel, K.: A review of atmospheric gravity waves and travelling ionospheric disturbances: 1982-1995,
631 *Ann. Geophys.*, 14, 917–940, <https://doi.org/10.1007/s00585-996-0917-6>, 1996.

632 Inan, U., Piddyachiy, D., Peter, W., Sauvaud, J., and Parrot, M.: DEMETER satellite observations of lightning-induced
633 electron precipitation, *Geophys. Res. Lett.*, 34, L07103, <https://doi.org/10.1029/2006GL029238>, 2007.

634 Isaev, N. V., Sorokin, V. M., Chmyrev, V. M., and Serebryakova, O. N.: Ionospheric electric fields related to sea storms and
635 typhoons, *Geomag. Aeron.*, 42, 638–643, 2002.

636 Isaev, N. V., Kostin, V. M., Belyaev, G. G., Ovcharenko, O. Ya., and Trushkina, E. P.: Disturbances of the topside
637 ionosphere caused by typhoons, *Geomag. Aeron.*, 50, 243–255, <https://doi.org/10.1134/S001679321002012X>, 2010.

638 Karpov, I. V. and Kshevetskii, S. P.: Numerical study of heating the upper atmosphere by acoustic-gravity waves from local
639 source on the Earth’s surface and influence of this heating on the wave propagation conditions, *J. Atmos. Solar-Terr. Phys.*,
640 164, 89–96, <https://doi.org/10.1016/j.jastp.2017.07.019>, 2017.

641 Ke, F. Y., Qi, X. M., Wang, Y., and Liu, X. W.: Statistics of ionospheric responses to Southeast Asia’s typhoons during
642 2006-2018 using the rate of change in the TEC index, *Adv. Space Res.*, 66, 1724–1742,
643 <https://doi.org/10.1016/j.asr.2020.06.003>, 2020.

644 Kong, J., Yao, Y., Xu, Y., Kuo, C., Zhang, L., Liu, L., and Zhai, C.: A clear link connecting the troposphere and ionosphere:
645 ionospheric reponses to the 2015 Typhoon Dujan, *J. Geod.*, 91, 1087–1097, <https://doi.org/10.1007/s00190-017-1011-4>,
646 2017.

647 Krishnam Raju, D. G., Rao, M. S., Rao, B. M., Jogulu, C., Rao, C. P., and Ramanadham, R.: Infrasonic oscillations in the F_2
648 region associated with severe thunderstorms, *J. Geophys. Res.*, 86, 5873–5880,
649 <https://doi.org/10.1029/JA086iA07p05873>, 1981.

650 Kubota, M., Shiokawa, K., Ejiri, M. K., Otsuka, Y., Ogawa, T., Sakanoi, T., Fukunishi, H., Yamamoto, M., Fukao, S., Saito,
651 A.: Traveling ionospheric disturbances observed in the OI 630-nm nightglow images over Japan by using a Multipoint
652 Imager Network during the FRONT Campaign, *Geophys. Res. Lett.*, 27, 4037–4040,
653 <https://doi.org/10.1029/2000GL011858>, 2000.

654 Kuester, M. A., Alexander, M. J., and Ray, E. A.: A model study of gravity waves over Hurricane Humberto (2001), *J.*
655 *Atmos. Sci.*, 65, 3231–3246, <https://doi.org/10.1175/2008JAS2372.1>, 2008.

656 Li, W., Yue, J., Yang, Y., Li, Z., Guo, J., Pan, Y., and Zhang, K.: Analysis of ionospheric disturbances associated with
657 powerful cyclones in East Asia and North America, *J. Atmos. Solar-Terr. Phys.*, 161, 43–54,
658 <https://doi.org/10.1016/j.jastp.2017.06.012>, 2017.

659 Li, W., Yue, J., Wu, S., Yang, Y., Li, Z., Bi, J., and Zhang, K.: Ionospheric responses to typhoons in Australia during 2005–
660 2014 using GNSS and FORMOSAT-3/COSMIC measurements, *GPS Solutions*, 22, 61, <https://doi.org/10.1007/s10291-018-0722-1>, 2018.

662 Luo, Y., Chernogor, L. F., Garmash, K. P., Guo, Q., Rozumenko, V. T., Shulga, S. N., and Zheng, Y.: Ionospheric effects of
663 the Kamchatka meteoroid: Results from multipath oblique sounding, *J. Atmos. Solar-Terr. Phys.*, 207, 105336,
664 <https://doi.org/10.1016/j.jastp.2020.105336>, 2020.

665 Marple Jr., S. L.: *Digital spectral analysis: with applications*, Inc, Englewood Cliffs, Prentice-Hall, N. J., XX, 492 p.,
666 <https://doi.org/10.1121/1.398548>, 1987.

667 Mikhailova, G. A., Mikhailov, Yu. M., and Kapustina, O. V.: ULF-VLF electric fields in the external ionosphere over
668 powerful typhoons in Pacific Ocean, *Int. J. Geomag. Aeron.*, 2, 153–158,
669 <http://elpub.wdcb.ru/journals/ijga/v02/gai99321/gai99321.htm>, 2000.

670 Mikhailova, G. A., Mikhailov, Yu. M., and Kapustina, O. V.: Variations of ULF-VLF electric fields in the external
671 ionosphere over powerful typhoons in Pacific Ocean, *Adv. Space Res.*, 30, 2613–2618, [https://doi.org/10.1016/S0273-1177\(02\)80358-1](https://doi.org/10.1016/S0273-1177(02)80358-1), 2002.

673 Nickolaenko, A. P. and Hayakawa, M.: Heating of the lower ionosphere electrons by electromagnetic radiation of lightning
674 discharges, *Geophys. Res. Lett.*, 22, 3015–3018, <https://doi.org/10.1029/95gl01982>, 1995.

675 Okuzawa, T., Shibata, T., Ichinose, T., Takagi, K., Nagasawa, C., Nagano, I., Mambo, M., Tsutsui, M., and Ogawa, T.:
676 Short-period disturbances in the ionosphere observed at the time of typhoons in September 1982 by a network of HF
677 Doppler receivers, *J. Geomag. Geoelectr.*, 38, 239–266, <https://doi.org/10.5636/jgg.38.239>, 1986.

678 Otsuka, Y., Tani, T., Tsugawa, T., Ogawa, T., Saito, A.: Statistical study of relationship between medium-scale traveling
679 ionospheric disturbance and sporadic E layer activities in summer night over Japan, *J. Atmos. Solar-Terr. Phys.*, 70, 2196–
680 2202, ISSN 1364-6826, <https://doi.org/10.1016/j.jastp.2008.07.008>, 2008.

681 Paulino, I., Medeiros, A. F., Vadas, S. L., Wrasse, C. M., Takahashi, H., Buriti, R. A., Leite, D., Filgueira, S., Bageston, J.
682 V., Sobral, J. H. A., and Gobbi, D.: Periodic waves in the lower thermosphere observed by OI630 nm airglow images, *Ann.*
683 *Geophys.*, 34, 293–301, <https://doi.org/10.5194/angeo-34-293-2016>, 2016.

684 Paulino, I., Moraes, J. F., Maranhão, G. L., Wrasse, C. M., Buriti, R. A., Medeiros, A. F., Paulino, A. R., Takahashi, H.,
685 Makela, J. J., Meriwether, J. W., and Campos, J. A. V.: Intrinsic parameters of periodic waves observed in the OI6300
686 airglow layer over the Brazilian equatorial region, *Ann. Geophys.*, 36, 265–273, <https://doi.org/10.5194/angeo-36-265-2018>,
687 2018.

688 Perkins, F. W.: Spread F and ionospheric currents. *J. Geophys. Res.* 78, 218–226. <https://doi.org/10.1029/JA078i001p00218>,
689 1973

690 Polyakova, A. S., and Perevalova, N. P.: Investigation into impact of tropical cyclones on the ionosphere using GPS
691 sounding and NCEP/NCAR reanalysis data, *Adv. Space Res.*, 48, 1196–1210. <https://doi.org/10.1016/j.asr.2011.06.014>,
692 2011.

693 Polyakova, A. S., and Perevalova, N. P.: Comparative analysis of TEC disturbances over tropical cyclone zones in the north-
694 west Pacific Ocean, *Adv. Space Res.*, 52, 1416–1426, <https://doi.org/10.1016/j.asr.2013.07.029>, 2013.

695 Prasad, S. S., Schneck, L. J., and Davies, K.: Ionospheric disturbances by severe tropospheric weather storms,
696 *J. Atmos. Terr. Phys.*, 37, 1357–1363, [https://doi.org/10.1016/0021-9169\(75\)90128-2](https://doi.org/10.1016/0021-9169(75)90128-2), 1975.

697 Pulnits, S. and Davidenko, D.: Ionospheric precursors of earthquakes and global electric circuit, *Adv. Space Res.*, 53, 709–
698 723, <https://doi.org/10.1016/j.asr.2013.12.035>, 2014.

699 Shiokawa, K., Ihara, C., Otsuka, Y., and Ogawa, T.: Statistical study of nighttime medium-scale traveling ionospheric
700 disturbances using midlatitude airglow images, *J. Geophys. Res.*, 108, 1052, doi:[10.1029/2002JA009491](https://doi.org/10.1029/2002JA009491), 2003.

701 Šindelářova, T., Burešová, D., Chum, J., and Hruška, F.: Doppler observations of infrasonic waves of meteorological origin
702 at ionospheric heights, *Adv. Space Res.*, 43, 1644–1651, <https://doi.org/10.1016/j.asr.2008.08.022>, 2009.

703 Song, Q., Ding, F., Zhang, X., Liu, H., Mao, T., Zhao, X., and Wang, Y.: Medium-scale traveling ionospheric disturbances
704 induced by Typhoon Chan-hom over China, *J. Geophys. Res.*, 124, 2223–2237, <https://doi.org/10.1029/2018JA026152>,
705 2019.

706 Sorokin, V. M., Isaev, N. V., Yaschenko, A. K., Chmyrev, V. M., and Hayakawa, M.: Strong DC electric field formation in
707 the low latitude ionosphere over typhoons, *J. Atmos. Solar-Terr. Phys.*, 67, 1269–1279,
708 <https://doi.org/10.1016/j.jastp.2005.06.014>, 2005.

709 Suzuki, S., Vadas, S. L., Shiokawa, K., Otsuka, Y., Karwamura, S., and Murayama, Y.: Typhoon-induced concentric airglow
710 structures in the mesopause region, *Geophys. Res. Lett.*, 40, 5983–5987,
711 <https://doi.org/10.1002/2013GL058087>, 2013.

712 Vadas, S. L., and Crowley, G.: Sources of the traveling ionospheric disturbances observed by the ionospheric TIDDBIT
713 sounder near Wallops Island on 30 October 2007. *J. Geophys. Res.*, 115, A07324, doi:[10.1029/2009JA015053](https://doi.org/10.1029/2009JA015053), 2010.

714 Vadas, S. L., Fritts, D. C., and Alexander, M. J.: Mechanism for the Generation of Secondary Waves in Wave Breaking
715 Regions. *Journal of the Atmospheric Sciences*, 60, 194–214. [https://doi.org/10.1175/1520-0469\(2003\)060<0194:MFTGOS>2.0.CO;2](https://doi.org/10.1175/1520-0469(2003)060<0194:MFTGOS>2.0.CO;2), 2003.

716

717 Vanina–Dart, L. B., Pokrovskaya, I. V., and Sharkov, E. A.: Studying the interaction between the lower equatorial
718 ionosphere and tropical cyclones according to data of remote and rocket sounding, *Izvestiya, Atmos. Oceanic Phys.*, 2, 19–
719 27, 2007.

720 Voss, H. D., Imhof, W. L., Walt, M., Mabilia, J., Gaines, E. E., Reagan, J. B., Inan, U. S., Helliwell, R. A., Carpenter, D. L.,
721 Katsufarakis, J. P., and Chang, H. C.: Lightning-induced electron precipitation, *Nature*, 312, 740–742,
722 <https://doi.org/10.1038/312740a0>, 1984.

723 Voss, H. D., Walt, M., Imhof, W. L., Mabilia, J., and Inan, U. S.: Satellite observations of lightning-induced electron
724 precipitation, *J. Geophys. Res.*, 103, 11,725–11,744, <https://doi.org/10.1029/97JA02878>, 1998.

725 Wen, Y. and Jin, S.: Traveling Ionospheric Disturbances Characteristics during the 2018 Typhoon Maria from GPS
726 Observations, *Remote Sens.*, 12, article #746, <https://doi.org/10.3390/rs12040746>, 2020.

727 Xiao, Z., Xiao, S.-G., Hao, Y.-Q., and Zhang, D.-H.: Morphological features of ionospheric response to typhoon,
728 *J. Geophys. Res.*, 112, A04304, <https://doi.org/10.1029/2006JA011671>, 2007.

729 Yiğit, E., Knížová, P. K., Georgieva, K., and Ward, W.: A review of vertical coupling in the Atmosphere–Ionosphere
730 system: Effects of waves, sudden stratospheric warmings, space weather, and of solar activity, *J. Atmos. Solar-Terr. Phys.*,
731 141, 1–12, <https://doi.org/10.1016/j.jastp.2016.02.011>, 2016.

732 Zakharov, V. I., and Kunitsyn, V. E.: Regional features of atmospheric manifestations of tropical cyclones according to
733 ground-based GPS network data, *Geomagn. Aeron.*, 52, 533–545, <https://doi.org/10.1134/S0016793212040160>, 2012.

734 Zakharov, V. I., Pilipenko, V. A., Grushin, V. A., and Khamidullin, A. F.: Impact of typhoon Vongfong 2014 on the
735 Ionosphere and Geomagnetic Field According to Swarm Satellite Data: 1. Wave Disturbances of Ionospheric Plasma, *Solar-*
736 *Terr. Physics.*, 5, 101–108, <https://doi.org/10.12737/stp-52201914>, 2019.

737 Zakharov, V. I. and Sigachev, P. K.: Ionospheric disturbances from tropical cyclones, *Adv. Space Res.*, 69, 132–141,
738 <https://doi.org/10.1016/j.asr.2021.09.025>, 2022.

739 Zhao, Y., Deng, Y., Wang, J.-S., Zhang, S.-R., and Lin, C. Y.: Tropical cyclone-induced gravity wave perturbations in the
740 upper atmosphere: GITM-R simulations, *J. Geophys. Res.*, 125, e2019JA027675, <https://doi.org/10.1029/2019JA027675>,
741 2020.

742 Zhao, Y. X., Mao, T., Wang, J. S., and Chen, Z.: The 2D features of tropical cyclone Usagi's effects on the ionospheric total
743 electron content, *Adv. Space Res.*, 62, 760–764, <https://doi.org/10.1016/j.asr.2018.05.022>, 2018.

744 Zheng, Y., Chernogor, L. F., Garmash, K. P., Guo, Q., Rozumenko, V. T., Luo, Y.: Disturbances in the ionosphere and
745 distortion of radio wave characteristics that accompanied the super typhoon Lekima event of 4–12 August 2019, *J. Geophys.*
746 *Res.*, 127, e2022JA030553, <https://doi.org/10.1029/2022JA030553>, 2022.

747